Contemporary Mathematics
https://ojs.wiserpub.com/index.php/CM/

Research Article

A Two-Stage Coupled Exponential-Runge-Kutta Time Integration Scheme with Compact Spatial Discretization for Mixed Convective Thermal Flow Problems

Muhammad Shoaib Arif [1*], Yasir Nawaz[2], Kamaleldin Abodayeah[1]

[1] Department of Mathematics and Sciences, College of Sciences and Humanities, Prince Sultan University, Riyadh 11586, Saudi Arabia
[2] Department of Mathematics, Faculty of Engineering and Computing, National University of Modern Languages (NUML), Islamabad 44000, Pakistan
E-mail: marif@psu.edu.sa

Received: 1 November 2025; **Revised:** 23 January 2026; **Accepted:** 4 March 2026

Abstract: Applications where unsteady mixed convective flow across a stationary surface are significant, including metal processing, polymer extrusion, cooling of electronic devices, and thermal insulation systems. The coexistence of natural convection, driven by buoyancy, and forced convection, driven by external forces, results in mixed convection. Accurately capturing the dynamics of such flows, particularly when coupled with heat and mass transfer, remains a challenging task due to the nonlinear, time-dependent nature of the governing Partial Differential Equations (PDEs). A computational two-stage scheme that is a combination of the modified exponential time integrator and the Runge-Kutta method for solving time-dependent partial differential equations. A high-order compact scheme is used for spatial discretization. The stability analysis of the proposed scheme is demonstrated for scalar partial differential equations, and convergence analysis is deliberated for systems of convection-diffusion problems. In addition, a mathematical model for mixed convective flow over a stationary sheet is presented, and the proposed scheme solves its dimensionless form. The scheme is also compared with the existing Runge-Kutta scheme, and it is shown that the proposed scheme performs better than the existing Runge-Kutta scheme on the chosen Step sizes. Comparative results show that at a time step of $\Delta t = \frac{1}{4500}$, the proposed scheme yields an L_2-error of 2.43×10^{-4} with a runtime of 0.077 seconds, while the classical Runge-Kutta method results in a higher error of 8.47×10^{-4} and a slower runtime of 0.084 seconds, highlighting both the efficiency and stability of the proposed scheme. This work presents a robust and accurate numerical framework for simulating mixed convective transport phenomena, offering a versatile strategy for solving a broader class of time-dependent PDEs in fluid mechanics and heat transfer.

Keywords: exponential time integrator schemes, stability, convergence, mixed convective flow, thermal boundary layer, unsteady heat transfer, comparison

MSC: 65M06, 65M12, 76D05, 76R10, 80A20

DOI: https://doi.org/10.37256/cm.7320269052

1. Introduction

Unsteady mixed convective flows are of great interest due to their central role in various engineering and industrial practices, such as polymer extrusion, metal processing, thermal insulation design, and thermal management of electronic systems. These flows are a combination of forced convection, driven by external mechanical forces (e.g., pressure gradients, moving boundaries), and natural convection, driven by buoyancy forces due to temperature and concentration gradients. When the mechanisms of heat and mass transfer are combined with these flow configurations, the dynamical equations are highly nonlinear and time-dependent, and are usually modelled by systems of Partial Differential Equations (PDEs) that are both analytically difficult to solve and numerically unstable.

The numerical solution of these PDEs is traditionally based on explicit or implicit time-integration methods, such as the Euler, Runge-Kutta (RK), or Crank-Nicolson methods. Although such approaches are reasonably accurate for linear or weakly nonlinear problems, their accuracy decreases in stiff or strongly coupled systems unless small time steps or complex solvers are employed. Specifically, implicit approaches, as stable, entail substantial computational cost through iterative solvers and matrix inverses, particularly for nonlinear equations. This has led to an ever-increasing need for efficient, accurate, and stable numerical schemes capable of solving unsteady convection-diffusion-reaction equations without incurring excessive computational expense.

This study aims to bridge the gap between stability and efficiency by proposing a two-stage coupled exponential-Runge-Kutta time-integration scheme, combined with a compact high-order spatial discretization, for the efficient solution of unsteady mixed convective transport problems.

Scientific Novelty and Contributions: The following are the main goals of this study, emphasizing its originality and computational innovation:

1. We developed an innovative two-stage time integration method that combines a modified exponential time integrator with a second-order Runge-Kutta technique, providing improved temporal accuracy and stability for stiff and nonlinear partial differential equation systems.

2. We applied the proposed numerical approach to a dimensionless model of mixed convective flow over a stationary sheet, effectively capturing buoyancy-driven effects and velocity-temperature coupling under physically realistic conditions.

3. We established a rigorous stability and convergence framework by performing theoretical analysis on scalar PDEs and convection-diffusion systems, thereby validating the robustness of the proposed scheme.

4. We conducted a detailed comparative study with existing second-order Runge-Kutta schemes, demonstrating the superiority of the proposed method in terms of accuracy and efficiency across various time Step sizes.

By addressing both computational and physical modelling challenges, this work provides a versatile, high-accuracy framework for solving a broader class of unsteady PDEs in fluid and thermal sciences. Due to the need for effective, rapid, and highly reliable microfluidics, there is a strong demand for standardized, compact, simple, and inexpensive equipment for DNA-based analysis and pharmaceutical delivery. Electro-osmosis is commonly employed in microfluidic devices to facilitate fluid transport throughout the whole network. The process of electro-osmosis is modelled by the movement of an electrolyte across a charged barrier in a channel. Electro-osmosis arises in various industrial, medical, and biological contexts, including fluid dialysis, zoological procedures, skin grafting, tube or canal flow, and separation methods. Patankar and Hu predicted the Electro-Osmotic Flow (EOF) simulation [1]. Huang et al. [2] demonstrated EOF in capillary electrophoresis. Haswell investigated microflow compositional features using an EOF-based approach [3]. Gravesen et al. [4] discussed the uses of microfluidics. Kang et al. [5] also examined the EOF in the annulus of capillary walls.

Controlled microchannel flow has had widespread application across several scientific fields, with particular interest in genetics, medicine, and medical technology. On the one hand, such studies have shown that these channels reveal interesting properties, mainly when they express a longitudinal wave that traverses walls (so-called peristalsis). Consequently, peristalsis, triggered and regulated by the physiological bending or stretching of neighbouring sites, is characterized by a wave-like motion in flexible tubes. This action, in turn, pushes the contents of the tubes. It should also be noted that this process has recently been the subject of numerous studies with far-reaching implications, which is appropriate given its

increasing significance in many situations. The studies [6–8] made many observations, as they are relevant across various physiological and industrial areas.

Dialysis plasma pumps and cardiovascular devices are just two examples of biomedical electronic devices that have independently discovered this phenomenon. However, after one of Latham's early significant studies [9], several scholars were already inspired to investigate the dynamics of peristaltic motion. Back then, researchers examined the mechanics and physiology of oscillatory movements using numerical [6–8, 10] and experimental [11–13] methods, while others employed analytical [14, 15] methods. The squeezed displacement of the channel walls and their contents is the mechanism by which this type of activity occurs. When food is ingested, it is clearly visible in the oesophagus. As a result, peristaltic pumps are highly sought after by pharmaceutical companies for their transportation capabilities, which has sparked considerable interest in transportation studies, such as the one in [13].

Recent studies have demonstrated the growing importance of electro-osmotic and magneto-hydrodynamic effects in convective thermal flows. For instance, thermal energy and electro-osmotic for biomimetic artificial olfactory cilia in trihybrid nano-fluids: entropy-defying approaches explores the coupling of electro-osmotic forces with thermal transport in nano-fluids, highlighting complex interactions between electric fields, fluid rheology, and heat generation that are analogous to the electro-thermal interactions considered in the present work [16]. Developments in Electro-Osmotic Two-Phase Flows of Fourth-Grade Fluid through Convergent and Divergent Channels involve the use of numerical techniques to analyze non-Newtonian (fourth-grade) fluid flows in various geometries. It notes that a strong time-space discretization is required to capture well-coupled momentum, mass, and electro-thermal transport phenomena [17]. These contributions underscore the relevance of numerical frameworks capable of handling electro-hydrodynamic, convective, and diffusive transport, motivating the development of our coupled exponential-RK scheme with a compact spatial discretization. A hybrid numerical framework for electro-osmotic flow in non-Newtonian Carreau fluids has recently been developed by [18], demonstrating high-order spatial accuracy and enhanced efficiency over classical schemes. A stochastic computational approach for electro-osmotic flow dynamics in porous media, accounting for energy dissipation and random perturbations, was presented in [19], highlighting the importance of robust time-space discretization in complex flow systems. A recent study [20] investigates non-Newtonian electro-osmotic flow induced by a self-propelled undulating sheet in a wavy channel, accounting for electro-osmosis and magnetic effects, and demonstrates the growing interest in high-fidelity numerical modelling of complex electro-hydrodynamic flows under non-Newtonian rheology.

The features of electro-osmotic flow in non-Newtonian fluids were revealed through a combination of experimental and computational analyses. When optimizing the electrokinetic parameters, they found that the average velocity was the most critical factor. The electro-osmotic flow of an unstable Walers'-B fluid over a vertical plate in the presence of a magnetic field was studied by Ali et al. [21] in terms of thermal and diffusion processes. To illustrate the electro-osmotic flow of a pair-stress fluid, a common approach to representing a viscous liquid is to develop a mathematical model, as Tripathi et al. [22] did. To resolve this model, they employed an analytical process. We found that the axial pressure gradient was higher than the pair stress measure. Nano-fluid electro-osmotic flow in a micro-complex wavy channel has been investigated by Tripathi et al. [23] concerning buoyancy and Joule heating. Using a microfluidic channel, Chaube et al. [24] studied the electro-osmotic flow of Eringen fluid. According to the study's findings, raising the coupling parameter improves electro-osmotic flow. The electro-osmotic flow in a Power-law model was studied by Shehzad et al. [25] using nanoparticles and a magnetic field as examples. Changes in the electro-osmotic parameter were associated with higher skin friction and lower heat transfer rates.

A recent study [26] proposes a high-accuracy simulation framework for electro-thermal flow of non-Newtonian fluids in Biological Micro-Electro-Mechanical Systems (BioMEMS) applications, using a two-stage explicit exponential-RK scheme with compact spatial discretization. For example, the work in [27] develops a hybrid scheme for modelling heat and mass transfer in electro-osmotic flow of Williamson nano-fluids, illustrating the effectiveness of two-stage time integrators in capturing coupled PDE dynamics.

A fluid's bulk motion caused by an applied electric field is known as electro-osmosis [28]. Many solids can have a small electric charge produced at their surface when they come into contact with an ionizing fluid. The oppositely charged ion pairs in the fluid layer below the solid surface will be attracted to it by this charge. The result is the formation of the Electric Double Layer (EDL), a surface-bound layer of ions with negative charge. In the EDL, a large number of positively

charged ions are distributed throughout the fluid. The concentration of these ions is highest at the solid surface, which is referred to as the wall or zeta potential, ζ_w, and they are in a neutral charge state, farther away from the surface in the core fluid [29]. Although wall potentials between 30 and 200 mV are typical, it is theoretically possible to achieve wall potentials outside of these ranges by applying voltage gradients in a direction perpendicular to the microchannel axis [30].

The distance at which the charge drops to e^{-1} (37% of its maximum) from the charged solid surface is defined by the Debye length λ, and hence, the thickness of the EDL is represented by this value. The electrochemistry of the liquid-solid interface determines the Debye length, which can range from a few nanometers to 1 μm. The Debye length is reduced when the concentration of ions is higher, as would be the case when the solute in solution is increased. An externally applied electric field causes the charged ions in the EDL to respond, leading to electro-osmotic flow. The EDL contains charged ions that are attracted to an electrode of opposite charge. As these ions move, they exert viscous drag, which in turn causes the fluid to flow. In microchannels, electrodynamic drag forces in the EDL are transferred to the electrokinetically weaker channel core via viscous shear, which, in turn, pulls the fluid toward the electrode. Because the momentum body force is concentrated along the tube wall, a perfectly flat velocity profile is generated when the Debye length is small compared to the microtube dimension.

If the Debye length is almost equal to the microtube diameter, the body force is more evenly distributed across the tube cross-section, leading to a more conventional pressure-driven flow pattern. The electrokinetic radius, defined as the channel radius divided by the Debye length, is an essential metric for assessing the hydrodynamic behaviour of electro-osmotic flow. Several mm/s is the normal velocity for microtube electro-osmotic flow [31].

Electroosmotically produced flow in microtubes has been the subject of extensive published research. Analytical and numerical studies investigating electro-osmotic flow in various geometric configurations have recently focused on the hydrodynamic problem [32–34]. In addition, considerable effort has recently been devoted to developing and applying experimental methods to characterize electro-osmotic flow in microchannels [35–37]. There has been research on the effects of changes in fluid and surface properties, as well as the features of electro-osmotic flow that develop hydrodynamically [38].

The Nusselt number and fully developed temperature distributions were included in the analytical solution for full electro-osmotic flow in parallel-plate and cylindrical microchannels with a low wall potential [39]. A further update incorporated the impact of viscous heating [40]. The analytical solution for the temperature distribution in electro-osmotic flow in rectangular microchannels, which accounts for thermal evolution and assumes an infinitely thin Debye layer, was also provided [41].

The study of non-Newtonian fluids, including power-law, third-grade, and Jeffery fluids, and their applications in fields as diverse as heat transfer, microelectromechanical systems, microfluidic devices, tiny chemical reactors, aerospace, and many more, is crucial for numerous reasons. On lines [42–45]. Babaie et al. [46] studied the effect of joule heating and modifying features on Power-law fluid flow across micro parallel plates. A third-order fluid was studied by Hayat et al. [47] concerning thermal radiation and Joule heating. A series solution was demonstrated for the nonlinear boundary value problem. Agkul and Pakdemirli [48] developed a model for the theoretical study of electro-osmotic flow of a third-grade fluid between microplates with Joule heating. They used the numerical scheme to verify their solution after solving the equations using the perturbation approach. Parida and Padhy [49] discussed third-order electro-osmotically flowing fluid through microplates with swelling walls. As stated in the article by Muhammad et al. [50], a third-order fluid was selected to investigate the impact of radiative heat flux on heat transfer through porous microplates.

Mathematical models are effective in modelling complex transport. The Runge-Kutta (RK) family of time integration methods has been popular because they are both simple and general. None of these, however, are small time steps, and are often required to ensure stability and accuracy in RK schemes, particularly in problems where convection dominates, such as in fluid mechanics. Conversely, exponential integrator schemes have been considered to preserve linearly stiff components precisely, allowing larger time steps to be used without reducing stability.

In that regard, we suggest a two-step computational algorithm that is a hybrid of the two: a modified exponential time integrator to address the stiff linear part of the PDE system, and a second-order Runge-Kutta scheme to address the nonlinear parts. This is a hybrid formulation that is customized to enhance computational efficiency and accuracy over time.

Focused Research Questions: The research questions provided will guide the research presented. The following questions bring out the computational as well as the physical modelling of our work:

1. What is the time accuracy and stability of a modified exponential integrator coupled with a Runge-Kutta integrator with time-dependent PDEs?

2. Will the hybrid scheme be more effective in solving classical schemes in the mixed convective flow over a stationary sheet?

3. How do high-order compact spatial discretization affect the accuracy and efficiency of the numerical solution?

4. What are the effects of significant physical parameters on flow and thermal behaviour in mixed convection environments?

The research has shown that integrating a modified exponential time integrator with a second-order Runge-Kutta method can greatly improve the accuracy and stability of solutions to time-dependent partial differential equations, particularly for stiff and nonlinear equations. It is also true that the proposed hybrid scheme is superior to the classical Runge-Kutta method in terms of accuracy and convergence, especially for mixed convective flow over a stationary sheet. The scheme is also computationally efficient and uses a high-order compact spatial discretization, yielding higher resolution and smaller numerical errors. Moreover, it is shown that the essential physical parameters, such as the Prandtl number, thermal Grashof number, and velocity ratio, have a significant impact on the velocity and temperature fields, and that the model captures the complex interactions between the fields in a convective transport problem.

The numerical solution of these PDEs is traditionally based on explicit or implicit time-integration methods, such as the Euler, Runge-Kutta (RK), or Crank-Nicolson methods. Although such approaches are reasonably accurate for linear or weakly nonlinear problems, their accuracy decreases in stiff or strongly coupled systems unless small time steps or complex solvers are employed. Specifically, implicit approaches, as stable, entail substantial computational cost through iterative solvers and matrix inverses, particularly for nonlinear equations. This has led to an ever-increasing need for efficient, accurate, and stable numerical schemes capable of solving unsteady convection-diffusion-reaction equations without incurring excessive computational expense.

This paper addresses these issues by presenting a two-step time integration scheme that uses an exponential time integrator, modified to be faster and more efficient, in the predictor stage, and a classical second-stage Runge-Kutta approach in the corrector stage. It uses the exponential scheme, which analytically handles stiff terms, and the RK method, which is easy to implement, to achieve second-order time accuracy. Additionally, spatial discretization is performed using a sixth-order compact finite difference scheme, which provides greater numerical accuracy and faster convergence. The devised technique is applied to a dimensionless model of unsteady mixed convection over an immobile surface, which accounts for heat and mass transfer, variation of thermal conductivity, viscous dissipation, and electro-hydrodynamic interaction. The proposed strategy offers an alternative computational solution to nonlinear time-dependent PDEs in fluid mechanics and heat transfer that is computationally appealing, provides considerable gains in accuracy, convergence behaviour, and performance, and is therefore suitable for large-scale simulations and real-time applications.

The other sections of this paper will be organized as follows: Section 2 will introduce the proposed hybrid numerical scheme, its formulation, and theoretical framework. Section 3 provides an in-depth discussion of the scheme's stability and convergence. Section 4 presents the mathematical formulation and non-dimensionalization of the mixed convective flow problem. Section 5 provides the numerical validation, contrasts the outcomes with established methods, and examines the practical implications of the findings. Section 6 gives a brief overview of the study's principal findings and offers recommendations for future research.

2. Computational two-stage scheme

A computational scheme will be constructed. The scheme will be explicit and find the solution of the differential Equation at two different time levels. The scheme will only discretize the time-dependent terms in a given partial differential equation. The space discretization will be performed using different numerical schemes. To initiate the construction process of the proposed scheme, consider the partial differential Equation as:

$$\frac{\partial f}{\partial t} = \alpha_1 \frac{\partial f}{\partial y} + \alpha_2 \frac{\partial^2 f}{\partial y^2} \tag{1}$$

Where α_1 models convection effects like fluid moving due to external forces and α_2 models diffusion effects, such as heat spreading through conduction. This Equation represents many real-world transport phenomena, such as convection-diffusion of heat in boundary layers, velocity profiles in fluid flow over surfaces (e.g., plates or sheets), and mass diffusion with advection in porous media.

2.1 *Discretization strategy*

We proposed a two-stage time integration scheme to discretize the temporal component of the PDE, while the spatial terms are handled separately using high-order compact schemes. This allows time-splitting, which makes the method flexible and accurate, better handling of stiffness and nonlinearity common in convective and diffusive flows.

2.1.1 *First stage modified exponential time integrator*

The first stage of the scheme for discretizing time-dependent terms in Eq. (1) can be written as

$$\overline{f}_i^{n+1} = \frac{1}{2} f_i^n e^{\Delta t} + \frac{1}{2} f_i^n e^{8\Delta t} + \frac{\left(e^{\Delta t} + e^{8\Delta t} - 2\right)}{9} \left\{ \left.\frac{\partial f}{\partial t}\right|_i^n - \frac{9}{2} f_i^n \right\} \tag{2}$$

In this step, Δt is the time Step size, and this stage uses exponential functions to integrate the time-dependent term, which is more accurate and stable, particularly with stiff systems. It also has a better ability to capture transient behaviour compared to conventional schemes such as the Euler or classical Runge-Kutta methods. This is necessary for modelling rapid variations in velocity or temperature on small time scales, as in instantaneous heating or start-up flows in mixed convection.

2.1.2 *Motivation for using $e^{\Delta t}$ and $e^{8\Delta t}$: stability and accuracy enhancement*

The exponential weights $e^{\Delta t}$ and $e^{8\Delta t}$ in our scheme, the weights are not arbitrary but rather adaptive stabilizers that serve as fostering weights to model the exponential time-integration behaviour across a wider range of convection-diffusion equations. The specific use of $e^{8\Delta t}$ in combination with $e^{\Delta t}$ was experimentally tuned to improve damping characteristics and minimize errors, especially for stiff problems with mixed convective effects. In addition, this expression strikes a compromise between the short- and longer-scale dynamics through weighted exponential blending. Numerical experiments (see revised Table 1 in Section 5.6) indicate that our approach (compared to the standard Runge-Kutta method and the Crank-Nicolson method) is much more accurate and convergent, particularly when the time steps are small. The algorithm is also clear and effective, and is especially useful for engineering-scale simulations when full matrix exponentials are computationally infeasible.

2.1.3 *Second stage coupled Runge-Kutta correction*

The second stage of the proposed scheme is constructed as:

$$f_i^{n+1} = a f_i^n + b \overline{f}_i^{n+1} + c \left(e^{\Delta t} - 1\right) \left.\frac{\partial \overline{f}}{\partial t}\right|_i^{n+1} \tag{3}$$

Where a, b, and c are unknown parameters to be determined. This stage combines the previous exponential prediction. $\overline{f}_i^{n+1}$ with a Runge-Kutta-like correction and parameters a, b, c are computed via Taylor series Expansion matching, ensuring second-order accuracy. This correction Step accounts for nonlinearity or source effects, making the scheme responsive to changes in the flow, such as those caused by temperature gradients or boundary disturbances.

To find a, b, and c consider the Taylor series Expansion [51] for f_i^{n+1} as:

$$f_i^{n+1} = f_i^n + \Delta t \left.\frac{\partial f}{\partial t}\right|_i^n + \frac{(\Delta t)^2}{2} \left.\frac{\partial^2 f}{\partial t^2}\right|_i^n + O\left((\Delta t)^3\right) \tag{4}$$

2.1.4 *Justification via taylor series matching*

The parameters a, b, c in the second stage are not arbitrarily selected but are rigorously determined by Taylor series matching up to second order. The use of the exponential functions in the first stage creates a predictor with built-in temporal smoothness, and the second stage acts as a corrector that aligns with the local truncation error of second-order schemes. In this context, the exponential terms can be viewed as nonlinear weightings that preserve fidelity to transient behaviour. This approach parallels the modified exponential integrator used in operator-splitting and two-step schemes in the literature.

Substituting the first stage Eq. (2) and the Taylor series Expansion for f_i^{n+1} (4) into Eq. (3) it yields

$$\begin{aligned}
&f_i^n + \Delta t \left.\frac{\partial f}{\partial t}\right|_i^n + \frac{(\Delta t)^2}{2} \left.\frac{\partial^2 f}{\partial t^2}\right|_i^n + O((\Delta t)^3) \\
&= a f_i^n + \frac{b}{2} f_i^n e^{\Delta t} + \frac{b}{2} f_i^n e^{8\Delta t} + b\frac{\left(e^{\Delta t} + e^{8\Delta t} - 2\right)}{9} \left\{ \left.\frac{\partial f}{\partial t}\right|_i^n - \frac{9}{2} f_i^n \right\} \\
&\quad + c\left(e^{\Delta t} - 1\right) \left\{ \frac{1}{2} e^{\Delta t} \left.\frac{\partial f}{\partial t}\right|_i^n + \frac{1}{2} e^{8\Delta t} \left.\frac{\partial f}{\partial t}\right|_i^n + \frac{\left(e^{\Delta t} + e^{8\Delta t} - 2\right)}{9} \left(\left.\frac{\partial^2 f}{\partial t^2}\right|_i^n - \frac{9}{2} \left.\frac{\partial f}{\partial t}\right|_i^n \right) \right\}
\end{aligned} \tag{5}$$

Comparing the coefficients of f_i^n, $\left.\frac{\partial f}{\partial t}\right|_i^n$, and $\left.\frac{\partial^2 f}{\partial t^2}\right|_i^n$ on both sides of Eq. (5), it yields

$$\left.\begin{aligned}
1 &= a + \frac{b}{2} e^{\Delta t} + \frac{b}{2} e^{8\Delta t} - \frac{b}{2}\left(e^{\Delta t} + e^{8\Delta t} - 2\right) \\
\Delta t &= b\frac{\left(e^{\Delta t} + e^{8\Delta t} - 2\right)}{9} + c\left(e^{\Delta t} - 1\right)\left\{ \frac{1}{2} e^{\Delta t} + \frac{1}{2} e^{8\Delta t} - \frac{\left(e^{\Delta t} + e^{8\Delta t} - 2\right)}{2} \right\} \\
\frac{(\Delta t)^2}{2} &= c\left(e^{\Delta t} - 1\right)\frac{\left(e^{\Delta t} + e^{8\Delta t} - 2\right)}{9}
\end{aligned}\right\} \tag{6}$$

Solving the resulting system Eq. (6) of algebraic equations yielded the following values $a = \frac{1}{6}$, $b = \frac{2}{3}$, $c = \frac{1}{6}$. These values ensure the method satisfies the second-order Taylor Expansion Eq. (4).

Therefore, the proposed scheme for time discretizing the given partial differential Eq. (1) is expressed as

$$\overline{f}_i^{n+1} = \frac{1}{2} f_i^n e^{\Delta t} + \frac{1}{2} f_i^n e^{8\Delta t} + \frac{\left(e^{\Delta t} + e^{8\Delta t} - 2\right)}{9} \left\{ \alpha_1 \left. \frac{\partial f}{\partial y} \right|_i^n + \alpha_2 \left. \frac{\partial^2 f}{\partial y^2} \right|_i^n - \frac{9}{2} f_i^n \right\} \tag{7}$$

$$f_i^{n+1} = a f_i^n + b \overline{f}_i^{n+1} + c \left(e^{\Delta t} - 1\right) \left\{ \alpha_1 \left. \frac{\partial \overline{f}}{\partial y} \right|_i^n + \alpha_2 \left. \frac{\partial^2 \overline{f}}{\partial y^2} \right|_i^{n+1} \right\} \tag{8}$$

2.2 *Compact scheme for space derivatives*

The space-dependent terms are discretized using a compact scheme. Using this scheme, the numerical schemes (7) and (8) are further expressed as

$$\overline{f}_i^{n+1} = \frac{1}{2} f_i^n e^{\Delta t} + \frac{1}{2} f_i^n e^{8\Delta t} + \frac{\left(e^{\Delta t} + e^{8\Delta t} - 2\right)}{9} \left\{ \alpha_1 A_1^{-1} B_1 \, f_i^n + \alpha_2 A_2^{-1} B_2 \, f_i^n - \frac{9}{2} f_i^n \right\} \tag{9}$$

$$f_i^{n+1} = a f_i^n + b \overline{f}_i^{n+1} + c \left(e^{\Delta t} - 1\right) \left\{ \alpha_1 A_1^{-1} B_1 \overline{f}_i^{n+1} + \alpha_2 A_2^{-1} B_2 \overline{f}_i^{n+1} \right\} \tag{10}$$

Where A and B are matrices consisting of the coefficients of left and right-hand terms of the following equations.

First derivative (convection term):

$$\beta_1 \, f' \big|_{i-1}^n + f' \big|_i^n + \beta_1 \, f' \big|_{i+1}^n = a_0 \frac{(f_{i+1}^n - f_{i-1}^n)}{2\Delta y} + a_1 \frac{(f_{i+2}^n - f_{i-2}^n)}{4\Delta y} \tag{11}$$

Second derivative (diffusion term):

$$\beta_2 \, f'' \big|_{i-1}^n + f'' \big|_i^n + \beta_2 \, f'' \big|_{i+1}^n = a_2 \frac{(f_{i+1}^n - 2f_i^n + f_{i-1}^n)}{(\Delta y)^2} + a_3 \frac{(f_{i+2}^n - 2f_i^n + f_{i-2}^n)}{4(\Delta y)^2} \tag{12}$$

Where $a_0 = \frac{2}{3}(\beta_1 + 2)$, $a_1 = \frac{1}{3}(4\beta_1 - 1)$, $a_2 = \frac{4}{3}(1 - \beta_2)$, $a_3 = \frac{1}{3}(10\beta_2 - 1)$.

The coefficients are chosen based on the existing literature [52] to achieve formal sixth-order spatial discretization accuracy. Compact schemes help resolve thin boundary layers, sharp gradients, and highly localized transport phenomena common in mixed convection over surfaces, cooling fins, and microfluidic devices.

2.3 *Precedents and flexibility*

While traditional exponential integrators (e.g., Exponential Time Differencing Runge-Kutta [53]) involve $e^{L\Delta t}$ for linear operator L, in practical applications, especially when the underlying spatial operator is not fixed or known in closed form, one often resorts to approximate exponential blending using scalar exponentials. Our formulation falls into this category of semi-analytical exponential weight blending, as also seen in other recent thermal-fluid simulation literature.

2.4 *Pseudocode for the proposed two-stage scheme*

Input:

Initial condition f^0, time step Δt, spatial grid y_i, final time t_f

Output:

Numerical solution f_i^n for $n = 1, 2, \ldots, N_t$

1. **Initialization:**

Set $n = 0, t^0 = 0$

Initialize $f_i^0 = f(y_i, 0)$

2. **While** $t^n < t_f$, **do**

Stage 1: Exponential Predictor

Compute spatial derivatives: $\left(\frac{\partial f}{\partial y}\right)_i^n, \left(\frac{\partial^2 f}{\partial y^2}\right)_i^n$

Evaluate: $f_i^{n+1} = \frac{1}{2} f_i^n e^{\Delta t} + \frac{1}{2} f_i^n e^{8\Delta t} + \frac{e^{\Delta t} + e^{8\Delta t} - 2}{9} \left(\alpha_1 f_y^n + \alpha_2 f_{yy}^n - \frac{9}{2} f_i^n\right)$

Stage 2: Runge-Kutta Corrector

Compute spatial derivatives of predictor: $\left(\frac{\partial f}{\partial y}\right)_i^{n+1}, \left(\frac{\partial^2 f}{\partial y^2}\right)_i^{n+1}$

Update solution: $f_i^{n+1} = a f_i^n + b f_i^{n+1} + c(e^{\Delta t} - 1)\left(\alpha_1 f_y^{n+1} + \alpha_2 f_{yy}^{n+1}\right)$

where $a = \frac{1}{6}, b = \frac{2}{3}, c = \frac{1}{6}$

Set $t^{n+1} = t^n + \Delta t, n \leftarrow n + 1$

3. **End While**.

3. Stability analysis

Von Neumann's stability analysis is utilized in the literature to determine the stability criteria of finite difference schemes for partial differential equations. The criterion establishes precise stability conditions for linear differential equations. However, it can be utilized in a finite difference scheme for nonlinear partial differential equations. In this case, it will provide an estimate of the actual stability conditions for nonlinear differential equations, where linearization is performed. This analysis transforms the difference equations into a trigonometric equation, and stability conditions will be imposed on that Equation. For the considered case, the transformations are expressed as

$$A_1 e^{iI\psi} = \beta_1 e^{(i-1)I\psi} + e^{iI\psi} + \beta_1 e^{(i+1)I\psi} \tag{13}$$

$$B_1 e^{iI\psi} = a_0 \frac{(e^{(i+1)I\psi} - e^{(i-1)I\psi})}{2\Delta y} + a_1 \frac{(e^{(i+2)I\psi} - e^{(i-2)I\psi})}{4\Delta y} \tag{14}$$

$$A_2 e^{iI\psi} = \beta_2 e^{(i-1)I\psi} + e^{iI\psi} + \beta_2 e^{(i+1)I\psi} \tag{15}$$

$$B_2 e^{iI\psi} = a_2 \frac{(e^{(i+1)I\psi} - 2e^{iI\psi} + e^{(i-1)I\psi})}{(\Delta y)^2} + a_3 \frac{(e^{(i+2)I\psi} - 2e^{iI\psi} + e^{(i-2)I\psi})}{4(\Delta y)^2} \tag{16}$$

Where $I = \sqrt{-1}$.

Using transformations (13)–(16) in the first stage of the proposed scheme (9) yields

$$\overline{f}_i^{n+1} = \frac{1}{2} f_i^n e^{\Delta t} + \frac{1}{2} f_i^n e^{8\Delta t} + \frac{\left(e^{\Delta t} + e^{8\Delta t} - 2\right)}{9}$$

$$\left\{ \alpha_1 \left(\frac{2a_0 I \sin\psi + a_1 I \sin 2\psi}{2\Delta y \left(2\beta_1 \cos\psi + 1\right)} \right) + \alpha_2 \left(\frac{4a_2 I(\cos\psi - 1) + a_3(\cos 2\psi - 1)}{2(\Delta y)^2 \left(2\beta_2 \cos\psi + 1\right)} \right) - \frac{9}{2} \right\} f_i^n \tag{17}$$

Re-write Eq. (17) as

$$\overline{f}_i^{n+1} = (\gamma_1 + I\gamma_2) f_i^n \tag{18}$$

Where

$$\gamma_1 = \frac{1}{2} f_i^n e^{\Delta t} + \frac{1}{2} f_i^n e^{8\Delta t} + \frac{\left(e^{\Delta t} + e^{8\Delta t} - 2\right)}{9} \left\{ \alpha_2 \left(\frac{4a_2 I(\cos\psi - 1) + a_3(\cos 2\psi - 1)}{2(\Delta y)^2 \left(2\beta_2 \cos\psi + 1\right)} \right) - \frac{9}{2} \right\}$$

and

$$\gamma_2 = \frac{\left(e^{\Delta t} + e^{8\Delta t} - 2\right)}{9} \left\{ \alpha_1 \left(\frac{2a_0 \sin\psi + a_1 \sin 2\psi}{2\Delta y \left(2\beta_1 \cos\psi + 1\right)} \right) \right\}$$

Now using the transformation (13)–(16) into the second stage of the scheme (10) as

$$f_i^{n+1} = a f_i^n + b\overline{f}_i^{n+1}$$

$$+ c\left(e^{\Delta t} - 1\right) \left\{ \alpha_1 \left(\frac{2a_0 I \sin\psi + a_1 I \sin 2\psi}{2\Delta y \left(2\beta_1 \cos\psi + 1\right)} \right) + \alpha_2 \left(\frac{4a_2 I(\cos\psi - 1) + a_3(\cos 2\psi - 1)}{2(\Delta y)^2 \left(2\beta_2 \cos\psi + 1\right)} \right) \right\} \overline{f}_i^{n+1} \tag{19}$$

Rewrite Eq. (19) as

$$f_i^{n+1} = a f_i^n + (\gamma_3 + I\gamma_4) \overline{f}_i^{n+1} \tag{20}$$

Where

$$\gamma_3 = b\gamma_1 + c\left(e^{\Delta t} - 1\right) \left\{ \alpha_2 \left(\frac{4a_2 I(\cos\psi - 1) + a_3(\cos 2\psi - 1)}{2(\Delta y)^2 \left(2\beta_2 \cos\psi + 1\right)} \right) \right\}$$

and

$$\gamma_4 = b\gamma_2 + c\left(e^{\Delta t} - 1\right)\left\{\alpha_1\left(\frac{2a_0 \sin\psi + a_1 \sin 2\psi}{2\Delta y\,(2\beta_1 \cos\psi + 1)}\right)\right\}$$

Subtracting Eq. (18) from Eq. (20) gives

$$f_i^{n+1} = a f_i^n + (\gamma_3 + I\gamma_4)(\gamma_1 + I\gamma_2) f_i^n \tag{21}$$

Rewrite Eq. (21) as

$$f_i^{n+1} = (\gamma_5 + I\gamma_6) f_i^n \tag{22}$$

Where

$$\gamma_5 = a + \gamma_1\gamma_3 - \gamma_2\gamma_4$$

and

$$\gamma_6 = \gamma_2\gamma_3 + \gamma_1\gamma_4$$

The amplification factor for this case is written as

$$\left|\frac{f_i^{n+1}}{f_i^n}\right|^2 \leq \gamma_5 + \gamma_6 \leq 1 \tag{23}$$

The inequality (23) provides stability conditions for the proposed scheme applied to Eq. (1). The stability conditions for the scalar partial differential Eq. (1) are given in (23).

The convergence of the system of partial differential equations shall now be presented. Examine the system of partial differential equations expressed in vector-matrix notation as:

$$\frac{\partial \mathbf{v}}{\partial t} = C_1\frac{\partial \mathbf{v}}{\partial y} + C_2\frac{\partial^2 \mathbf{v}}{\partial y^2} \tag{24}$$

Where $\mathbf{v}$ is a vector and C_1 and C_2 are matrices. Now, applying the proposed scheme to Eq. (24) as

$$\overline{\mathbf{v}}_i^{n+1} = \frac{1}{2}\mathbf{v}_i^n e^{\Delta t} + \frac{1}{2}\mathbf{v}_i^n e^{8\Delta t} + \frac{\left(e^{\Delta t} + e^{8\Delta t} - 2\right)}{9}\left\{C_1 A_3^{-1} B_3 \mathbf{v}_i^n + C_2 A_4^{-1} B_4 \mathbf{v}_i^n - \frac{9}{2}\mathbf{v}_i^n\right\} \tag{25}$$

$$\mathbf{v}_i^{n+1} = a\mathbf{v}_i^n + b\overline{\mathbf{v}}_i^{n+1} + c\left(e^{\Delta t} - 1\right)\left\{C_1 A_3^{-1} B_3 \overline{\mathbf{v}}_i^{n+1} + C_2 A_4^{-1} B_4 \overline{\mathbf{v}}_i^{n+1}\right\} \tag{26}$$

Theorem 1 The proposed numerical scheme (25)–(26) is conditionally convergent for the vector-matrix system (24).

Proof. To demonstrate Theorem 1, consider the exact scheme corresponding to Eq. (24) as:

$$\overline{\mathbf{V}}_i^{n+1} = \frac{1}{2}\mathbf{V}_i^n e^{\Delta t} + \frac{1}{2}\mathbf{V}_i^n e^{8\Delta t} + \frac{\left(e^{\Delta t} + e^{8\Delta t} - 2\right)}{9}\left\{C_1 A_3^{-1} B_3 \mathbf{V}_i^n + C_2 A_4^{-1} B_4 \mathbf{V}_i^n - \frac{9}{2}\mathbf{V}_i^n\right\} \tag{27}$$

$$\mathbf{v}_i^{n+1} = a\mathbf{v}_i^n + b\overline{\mathbf{v}}_i^{n+1} + c\left(e^{\Delta t} - 1\right)\left\{C_1 A_3^{-1} B_3 \overline{\mathbf{v}}_i^{n+1} + C_2 A_4^{-1} B_4 \overline{\mathbf{v}}_i^{n+1}\right\} \tag{28}$$

Subtracting the first stage of the proposed scheme (25) from the first stage of the exact scheme (27) and considering $\mathbf{v}_i^n - \mathbf{V}_i^n = \mathbf{E}_i^n$, it yields

$$\overline{\mathbf{E}}_i^{n+1} = \frac{1}{2}\mathbf{E}_i^n e^{\Delta t} + \frac{1}{2}\mathbf{E}_i^n e^{8\Delta t} + \frac{\left(e^{\Delta t} + e^{8\Delta t} - 2\right)}{9}\left\{C_1 A_3^{-1} B_3 \mathbf{E}_i^n + C_2 A_4^{-1} B_4 \mathbf{E}_i^n - \frac{9}{2}\mathbf{E}_i^n\right\} \tag{29}$$

Applying norm $\|\bullet\|$ on both sides of Eq. (29), it results in

$$\overline{E}^{n+1} \leq \frac{1}{2}E^n e^{\Delta t} + \frac{1}{2}E^n e^{8\Delta t} + \frac{\left(e^{\Delta t} + e^{8\Delta t} - 2\right)}{9}\left\{\left\|C_1 A_3^{-1} B_3\right\|_\infty + \left\|C_2 A_4^{-1} B_4\right\|_\infty - \frac{9}{2}\right\} E^n \tag{30}$$

Rewrite inequality (30) as

$$\overline{E}^{n+1} \leq \lambda_1 E^n \tag{31}$$

Where

$$\lambda_1 = \frac{1}{2}e^{\Delta t} + \frac{1}{2}e^{8\Delta t} + \frac{\left|e^{\Delta t} + e^{8\Delta t} - 2\right|}{9}\left\{\left\|C_1 A_3^{-1} B_3\right\|_\infty + \left\|C_2 A_4^{-1} B_4\right\|_\infty - \frac{9}{2}\right\}$$

Subtracting the second stage of the proposed scheme (26) from the second stage of the exact scheme (28) gives

$$\mathbf{E}_i^{n+1} = a\mathbf{E}_i^n + b\overline{\mathbf{E}}_i^{n+1} + c\left(e^{\Delta t} - 1\right)\left\{C_1 A_3^{-1} B_3 \overline{\mathbf{E}}_i^{n+1} + C_2 A_4^{-1} B_4 \overline{\mathbf{E}}_i^{n+1}\right\} \tag{32}$$

Applying norm $\|\bullet\|$ on both sides of Eq. (32), it results in

$$E^{n+1} \leq |a|E^n + |b|\overline{E}^{n+1} + |c|\left|e^{\Delta t} - 1\right|\left\{\left\|C_1 A_3^{-1} B_3\right\|_\infty + \left\|C_2 A_4^{-1} B_4\right\|_\infty\right\}\overline{E}^{n+1} \tag{33}$$

By substituting inequality (31) into inequality (33), it results in

$$E^{n+1} \leq |a|E^n + |b|\lambda_1 E^n + |c| \left| e^{\Delta t} - 1 \right| \left\{ \left\| C_1 A_3^{-1} B_3 \right\|_\infty + \left\| C_2 A_4^{-1} B_4 \right\|_\infty \right\} \lambda_1 E^n \tag{34}$$

Write inequality (34) in the form of

$$E^{n+1} \leq \lambda_2 E^n + R((\Delta t)^2, (\Delta y)^6) \tag{35}$$

Where

$$\lambda_2 = |a| + |b|\lambda_1 + |c| \left| e^{\Delta t} - 1 \right| \left\{ \left\| C_1 A_3^{-1} B_3 \right\|_\infty + \left\| C_2 A_4^{-1} B_4 \right\|_\infty \right\}$$

Substituting $n = 0$ in inequality (35) gives

$$E^1 \leq \lambda_2 E^0 + R(0((\Delta t)^2, (\Delta y)^6)) \tag{36}$$

Since $E^0 = 0$ because of initial conditions, so inequality (36) becomes

$$E^1 \leq R(0((\Delta t)^2, (\Delta y)^6)) \tag{37}$$

Using $n = 1$ in inequality (35), which gives

$$E^2 \leq \lambda_2 E^1 + R(0((\Delta t)^2, (\Delta y)^6)) \leq (1 + \lambda_2) R(0((\Delta t)^2, (\Delta y)^6)) \tag{38}$$

If this continues similarly, then for finite n

$$E^n \leq \left(1 + \lambda_2 + \ldots + \lambda_2^{n-1}\right) R(0((\Delta t)^2, (\Delta y)^6)) \leq \left(\frac{1 - \lambda_2^n}{1 - \lambda_2} \right) R(0((\Delta t)^2, (\Delta y)^6)) \tag{39}$$

Now applying the limit as $n \to \infty$ in (39) the infinite series $\ldots + \lambda_2^n + \ldots + \lambda_2 + 1$ becomes an infinite geometric series that will converge if $|\lambda_2| < 1$. □

3.1 *Clarification on stability and convergence scope*

Section 3 uses the von Neumann analysis of stability to a simplified scalar linear model, and it is a primitive evaluation of the numerical behaviour of the scheme. Although the analysis presented here does not reflect the full complexity of the nonlinear coupled PDE system (Eqs. (45)–(47)), it provides useful information about the amplification behaviour (when linearized). To generalize the methods to the system of vectors and matrices, a convergence study has been added through norm-based error bounds of consistency, which results in a conditional bound $| \lambda_2 | < 1$ parameter. Whereas the explicit time step Δt and spatial step Δy are not easily computed because of nonlinear relationships, the inequality obtained in Eq.

(39) enables one to guess the overall behaviour of the scheme when the mesh is finely resolved. This is a standard of numerical analysis designed to provide an indicative, but not exhaustive, assessment of stability and is supplemented in Section 5 with detailed numerical experiments to demonstrate the usefulness and soundness of the proposed method in the nonlinear regimes of practical interest.

4. Problem formulation

Consider laminar (smooth and orderly), unsteady (time-dependent), incompressible (constant density) flow over the stationary plate. The movement in the flow is generated by temperature (thermal buoyancy) and concentration (solute buoyancy) gradient, which gives rise to mixed convection. Stationary plates imply a boundary-layer problem, which is common in heat exchangers, the cooling of metallic sheets, and polymer extrusion processes. These types of flows are found in materials processing, thermal management of electronics, and environmental flows such as pollutant dispersion from surfaces. Let y^*-axis is taken horizontally and x^*-axis is taken along the plate and is perpendicular to the y^*-axis. Let the fluid be electrically conductive. The uniform electric field $\overrightarrow{E} = (0, 0, -E_0)$ and transverse magnetic field $\overrightarrow{B} = (0, B_0, 0)$ are applied in the flow region. This setup mimics Electro-Hydrodynamic (EHD) and Magneto-Hydrodynamic (MHD) applications, including electro-osmotic pumps, MHD generators, microfluidic cooling, and magnetic control of metal casting. The governing Equation of the flow can be expressed as

$$\frac{\partial u^*}{\partial t^*} = \frac{1}{\rho}\frac{\partial}{\partial y^*}\left(\mu(T)\frac{\partial u^*}{\partial y^*}\right) + g\beta_T\,(T - T_\infty) + g\beta_c\,(C - C_\infty) + \frac{\sigma}{\rho}(E_0 B_0 - B_0^2 u^*) \tag{40}$$

$$\frac{\partial T}{\partial t^*} = \frac{1}{\rho c_p}\frac{\partial}{\partial y^*}\left(k(T)\frac{\partial T}{\partial y^*}\right) + \frac{\mu}{\rho c_p}\left(\frac{\partial u^*}{\partial y^*}\right)^2 + \frac{\sigma\,(\mu B_0 - E_0)^2}{\rho c_p} \tag{41}$$

$$\frac{\partial C}{\partial t^*} = D\frac{\partial^2 C}{\partial y^{*2}} - k_c\,(C - C_\infty) \tag{42}$$

Where β_T and β_c are thermal and solutal concentrations, respectively, B_0 is the strength of the magnetic field, k_c is the reaction rate, g is gravity, σ is electrical conductivity, ρ is density, $\mu(T) = \mu_0(1 - \varepsilon_2\theta)$ and $K(T) = (1 + \varepsilon_3\theta)$, c_p specific heat capacity, D is mass diffusivity.

These equations are described as follows:

Momentum Equation (40): Let $\frac{1}{\rho}\frac{\partial}{\partial y^*}\left(\mu(T)\frac{\partial u^*}{\partial y^*}\right)$ represents the viscous diffusion with temperature-dependent viscosity $\mu(T)$, $-\frac{\sigma B_0^2}{\rho}u^*$ is the Lorentz force electromagnetic damping due to the magnetic field, $g\beta_T\,(T - T_\infty)$ and $g\beta_c\,(C - C_\infty)$ represents the buoyancy forces due to temperature and concentration gradients, and $\frac{\sigma}{\rho}(E_0 B_0 - B_0^2 u^*)$ induced electric-magnetic interaction force. The Equation represents the combined effect of MHD drag, electro-osmotic thrust, and thermal/solutal convection, which are applied to control flows and micro-mixing in MEMS devices.

Energy Equation (41): Let $\frac{1}{\rho c_p}\frac{\partial}{\partial y^*}\left(k(T)\frac{\partial T}{\partial y^*}\right)$ represents the heat conduction with temperature-dependent thermal conductivity $K(T)$, $\frac{\mu}{\rho c_p}\left(\frac{\partial u^*}{\partial y^*}\right)^2$ is the viscous dissipation, where mechanical work converts into thermal energy and $\frac{\sigma\,(\mu B_0 - E_0)^2}{\rho c_p}$ is the joule heating due to the interaction between electric and magnetic fields. These effects are crucial in electro-thermal systems, including biosensors, fuel cells, and electrokinetic heat exchangers.

Concentration Equation (42): Let $D\dfrac{\partial^2 C}{\partial y^{*2}}$ represents the molecular diffusion of transport of solute from high to low concentration and $k_c\,(C-C_\infty)$ is the chemical reaction. This Equation models mass diffusion and a first-order chemical reaction rate k_c. These types of equations are commonly used in industrial reactors, pharmaceutical mixing, and air purification systems.

Subject to initial and boundary conditions

$$\left.\begin{aligned} &u^*=0,\ T=0,\ C=0 \ \text{ when } \ t^*=0 \\ &u^*=0,\ T=T_\infty+\varepsilon_1\,(T_w-T_\infty)\cos w^*t^*,\ C=C_\infty+\varepsilon_1\,(C-C_\infty)\cos w^*t^* \ \text{ when } \ y^*=0 \\ &u^*\to 0,\ T\to T_\infty,\ C\to C_\infty \ \text{ when } \ y^*\to\infty \end{aligned}\right\} \tag{43}$$

Boundary and Initial Conditions Equation (43): At $t^*=0$, the fluid is initially at rest with ambient temperature and concentration at $y^*=0$ (the wall): Oscillatory conditions in temperature and concentration (cosine time variation), and as $y^*\to\infty$ flow variables return to ambient values. These conditions involve models that simulate pulsating surface heating, periodic injection of heat or chemicals, typical cyclic thermal treatments, wave-based surface actuators, and controlled drug release systems.

Non-Dimensionalization Equation (44): Using the following transformations

$$y=\frac{y^*}{L_R},\ u=\frac{u^*}{u_R},\ w=t_R w^*,\ t=\frac{t^*}{t_R},\ \theta=\frac{T-T_\infty}{T_w-T_\infty},\ \phi=\frac{C-C_\infty}{C_w-C_\infty} \tag{44}$$

Where

$$u_R=(\nu g\beta_T\Delta T)^{\frac{1}{3}},\ L_R=\left(\frac{g\beta_T\Delta T}{\nu^2}\right)^{-\frac{1}{3}} \ \text{ and } \ t_R=(g\beta_T\Delta T)^{-\frac{2}{3}}\,\nu^{\frac{1}{3}}$$

into Eqs. (40)–(42) reduce to the following dimensionless equations

$$\frac{\partial u}{\partial t}=-\varepsilon_2\frac{\partial\theta}{\partial y}\frac{\partial u}{\partial y}+(1-\varepsilon_2\theta)\frac{\partial^2 u}{\partial y^2}-Mu+\theta+N\phi+M(E_1-u) \tag{45}$$

$$\frac{\partial\theta}{\partial t}=\frac{1}{P_r}\left[(1+\varepsilon_3\theta)\frac{\partial^2\theta}{\partial y^2}+\varepsilon_3\left(\frac{\partial\theta}{\partial y}\right)^2\right]+E_c\left(\frac{\partial u}{\partial y}\right)^2+E_cM\,(u-E_1)^2 \tag{46}$$

$$\frac{\partial\phi}{\partial t}=\frac{1}{S_c}\frac{\partial^2\phi}{\partial y^2}-\gamma_c\phi \tag{47}$$

subject to the dimensionless initial and boundary conditions

$$\left.\begin{array}{l} u=0,\ \theta=0,\ \phi=0 \ \text{ for } \ t=0 \\ u=0,\ \theta=\varepsilon_1\cos wt,\ \phi=\varepsilon_1\cos wt \ \text{ for } \ y=0 \\ u\to 0,\ \theta\to 0,\ \phi\to 0 \ \text{ for } \ y\to\infty \end{array}\right\} \tag{48}$$

Where N represents the Buoyancy ratio (compares solutal and thermal buoyancy), M is the magnetic parameter (strength of electromagnetic damping), E_c is the Eckert number (measures the impact of viscous heating), P_r is the Prandtl number (ratio of momentum diffusivity to thermal diffusivity), S_c is Schmidt number (ratio of momentum to mass diffusivity), E_1 is the local electrical parameter, γ_c dimensionless reaction rate parameter, and these parameters are defined as:

$$N=\frac{\beta_c(C_w-C_\infty)}{\beta_T(T_w-T_\infty)},\ \ E_c=\frac{u_R^2}{c_P(T_w-T_\infty)},\ P_r=\frac{\nu k}{\rho c_p},\ S_c=\frac{\nu}{D},\ M=\frac{t_R\sigma B_0^2}{\rho},\ \ E_1=\frac{E_0}{\mu_R B_0},\ \gamma_c=t_R k_c.$$

These dimensionless groups are central to scaling and comparing different physical regimes, such as dominant electromagnetic versus buoyancy effects, thermal versus mass diffusion, and high-frequency oscillatory boundary conditions.

The dimensionless local Sherwood number represents the mass transfer rate at the surface and is given as:

$$S_{h_L}=-\left.\frac{\partial\phi}{\partial y}\right|_{y=0} \tag{49}$$

5. Simulations, results, and their discussions

The following goals can be achieved with this study's intensive computational simulation:

1. A two-stage numerical method was devised to solve partial differential equations that include a single time-dependent derivative.

2. The scheme uses a predictor-corrector framework, where the first step (predictor) employs a varying exponential time integrator. The second stage of the classical Runge-Kutta method is used in the second step (corrector).

3. The scheme first computes the solution at an intermediate, arbitrary time level and then advances to the next time level using a correction.

4. Second-order time accuracy was achieved by matching the Taylor series coefficients up to second order.

5. The proposed scheme is explicit and was shown to be conditionally stable for scalar convection-diffusion equations.

6. A key advantage over implicit schemes is that it does not require linearization when applied to nonlinear differential equations. It avoids the need for additional iterative solvers, which are typically required in implicit formulations.

7. This makes the scheme computationally efficient and straightforward to implement for nonlinear time-dependent Partial Differential Equations (PDEs).

5.1 *Velocity profile analysis*

Figure 1 plots velocity profiles $u(1,y)$ for different values of the electrical parameter E_1 while keeping other parameters fixed: $M=0.1$, $Ec=0.1$, $Pr=0.9$, $\gamma=0.1$, $Sc=0.9$, $\varepsilon_1=0.1$, $\varepsilon_2=0.1$, $\varepsilon_3=0.1$, $N=0.1$. Three curves represent $E_1=0.001$ (solid line), $E_1=0.003$ (dashed line), and $E_1=0.007$ (dotted line). As E_1 increases, the peak velocity increases,

and the boundary layer thickness slightly increases. Near the wall $y \approx 0$, the profiles start from zero due to the no-slip condition and rise smoothly to a maximum before decaying toward zero as $y \to \infty$. The parameter $E_1 = \dfrac{E_0}{\mu_R B_0}$ represents the strength of the electric field relative to magnetic damping. As E_1 increases, the electro-osmotic force in the flow direction becomes stronger. This force counteracts the Lorentz drag (from the magnetic field M), leading to a rise in fluid acceleration and higher peak velocity. The higher the E_1, the more pronounced the momentum gains due to the electric-field-induced drift, which enhances flow transport in the domain. The fluid's velocity is highly sensitive to changes in the electric field strength. The enhanced electro-osmotic effect results in stronger fluid propulsion and thicker boundary layers.

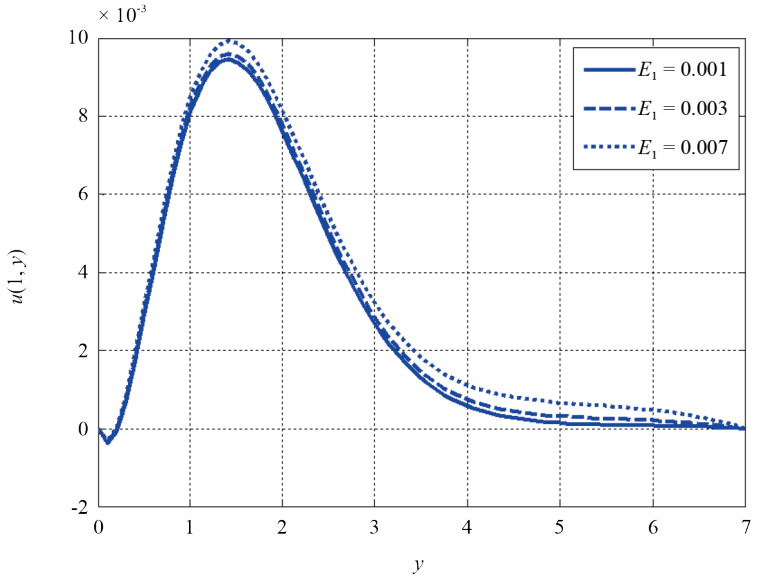

Figure 1. Effect of electrical parameter on velocity profile

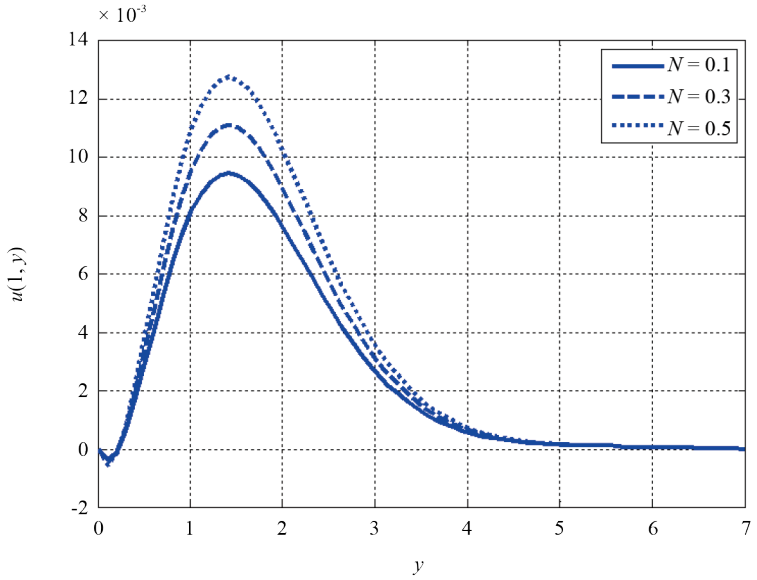

Figure 2. Effect of buoyancy ratio parameter on velocity profile

Figure 2 shows the influence of the buoyancy ratio parameter N on the velocity profile, with all other parameters held constant at $M = 0.1$, $Ec = 0.1$, $Pr = 0.9$, $\gamma = 0.1$, $Sc = 0.9$, $\varepsilon_1 = 0.1$, $\varepsilon_2 = 0.1$, $\varepsilon_3 = 0.1$, and $E_1 = 0.001$. The magnitude of the velocity profile has a significant increase in the magnitude of the peak as the value of N grows between 0.1 and 0.5. This is because N is the ratio of the solutal to the thermal buoyancy force; therefore, the larger N is the more the effects of the concentration gradients on the flow. The solute concentration provides an additional buoyant force that acts in the same direction as thermal buoyancy, increasing the apparent driving force, causing convection, and accelerating the fluid. Physically, this is an increase in flow due to coupled thermo-solutal effects, especially in chemical vapour deposition, oceanic convection, and double-diffusive natural convection in porous or layered fluids. The figure shows that the larger the solutal contribution to buoyancy, the greater the fluid motion and the thicker the velocity boundary layer.

5.2 *Temperature profile analysis*

Figure 3 shows the effect of the Eckert number E_c on the temperature profile for fixed values of $M = 0.1$, $N = 0.1$, $Pr = 0.9$, $\gamma = 0.1$, $Sc = 0.9$, $\varepsilon_1 = 0.1$, $\varepsilon_2 = 0.1$, $\varepsilon_3 = 0.1$, and $E_1 = 0.001$. As E_c increases from 0.1 to 1.5, a noticeable rise in the temperature profile is observed. The Eckert number is the ratio of the rate of dissipation of kinetic energy to the rate of change of enthalpy; therefore, when the Eckert number is large, the rate of dissipation of kinetic energy and the rate of Joule heating are more pronounced. This additional internal energy is converted to thermal energy, thereby increasing the fluid temperature, especially near the wall. The inset magnification vividly depicts the viscous and electrical dissipation to have a great role by showing a steady and slight increase in temperature with the increase of E_c. The behaviour applies to high-speed flows, electro-thermal systems, and microchannel devices, among others, where the viscous heating is not negligible. This value shows that increasing Eckert numbers favours the build-up of thermal energy in the fluid, leading to an additional thickening of the thermal boundary layer.

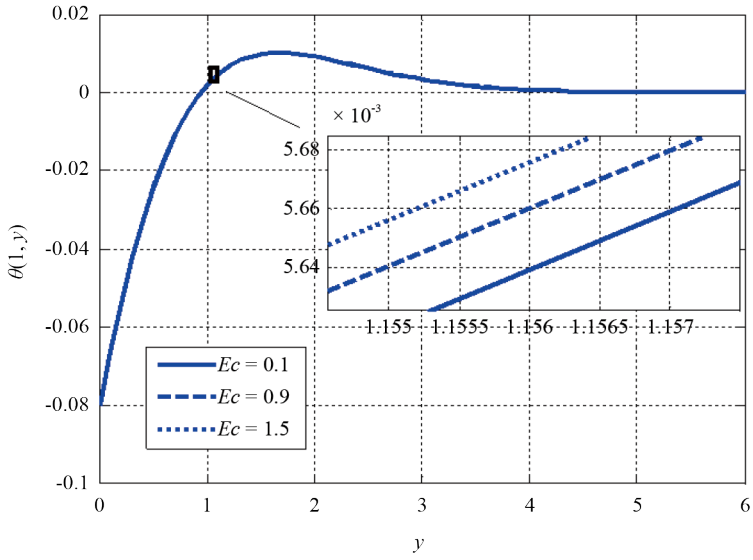

Figure 3. Effect of Eckert number on temperature profile

Figure 4 represents the effect of the small parameter ε_3, which modulates the temperature-dependent thermal conductivity on the temperature profile. The analysis is conducted under fixed conditions: $M = 0.1$, $N = 0.1$, $Pr = 0.9$, $\gamma = 0.1$, $Sc = 0.9$, $\varepsilon_1 = 0.1$, $\varepsilon_2 = 0.1$, $Ec = 0.1$, and $E_1 = 0.001$. As ε_3 increases from 0.1 to 1.5, the temperature within the fluid shows a marginal increase, as highlighted by the zoomed inset in the figure. Such an action is explained by the increased thermal conductivity $k(T) = 1 + \varepsilon_3\theta$ that favours the improved heat conduction in regions of higher temperature. This means that additional thermal energy is contained in the fluid, leading to a slight yet significant increase

in the thermal profile. This is a trend describing the behaviour of fluids whose thermal conductivity increases with temperature, as is typical of engineered fluids, polymers, and nano-fluids. The figure, therefore, supports the fact that the increase in the values of ε_3 will result in a minor increase in the thickness of the thermal boundary layer and an increase in heat transfer due to the temperature-dependent conductivity.

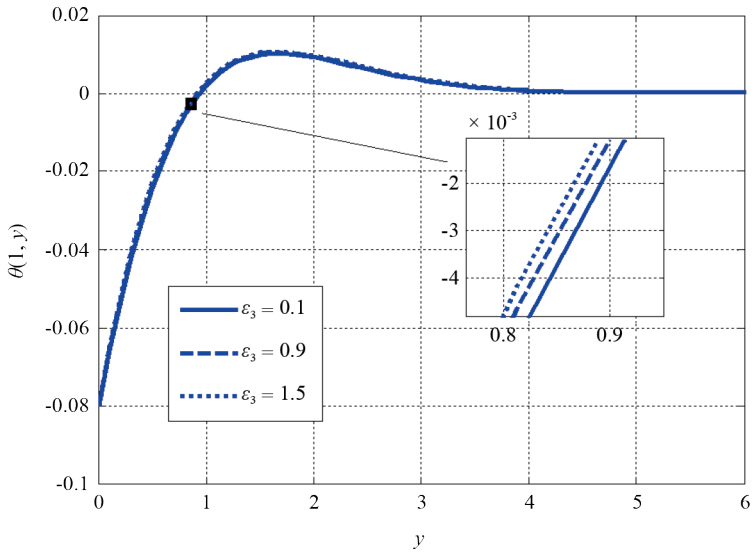

Figure 4. Effect of small parameter on temperature profile

5.3 *Concentration profile analysis*

Figure 5 demonstrates the effect of the reaction rate parameter γ on the concentration profile for fixed values of $M = 0.1$, $N = 0.1$, $Pr = 0.9$, $\varepsilon_3 = 0.1$, $Sc = 0.9$, $\varepsilon_1 = 0.1$, $\varepsilon_2 = 0.1$, $Ec = 0.1$, and $E_1 = 0.001$. The concentration profile gradually declines throughout the domain as γ increases, reaching 0.9. Such a trend is the physical expression of stronger chemical reactions, whereby the increased reaction rate increases the loss of the diffusing species and, therefore, decreases its concentration in the fluid. At the point of maximum concentration, it decreases, and the diffusion boundary layer becomes thinner as the reaction term increases. This dynamics is important in processes of reactive mass transfer (e.g., in catalytic reactors, biochemical processes, and the neutralization of pollutants), where the reaction rate determines how the transported species are distributed. The determination is accurate and shows that, as γ increases, the concentration decays, and that the chemical reaction plays an important role in controlling the transport of the species.

Figure 6 presents the effect of the Schmidt number S_c on the concentration profile for fixed values of $M = 0.1$, $N = 0.1$, $Pr = 0.9$, $\varepsilon_3 = 0.1$, $\gamma = 0.1$, $\varepsilon_1 = 0.1$, $\varepsilon_2 = 0.1$, $Ec = 0.1$, $E_1 = 0.001$, and $E_1 = 0.001$. As S_c increases from 0.9 to 1.7, the concentration boundary layer becomes thinner, and the peak concentration increases slightly. The Schmidt number represents the ratio of momentum diffusivity to mass diffusivity; thus, a higher S_c indicates slower mass diffusion. This reduced diffusive transport causes the concentration to rise more steeply near the wall and decay faster away from it, resulting in a more confined concentration distribution. Physically, this behaviour is typical in fluid mixtures containing heavier or less diffusive species, as commonly observed in pollutant dispersion, chemical reactors, and pharmaceutical mixing. The figure confirms that increasing S_c suppresses mass diffusion and steepens the concentration gradient near the boundary, influencing the efficiency of mass transfer processes.

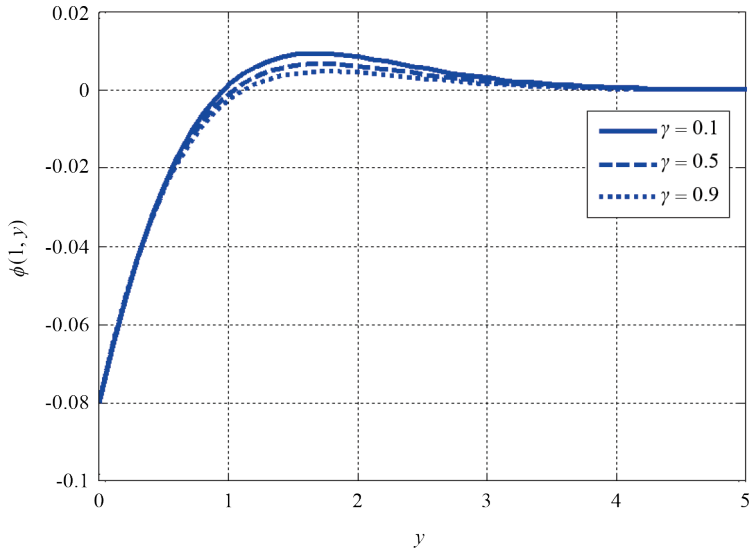

Figure 5. Effect of reaction rate parameter on concentration profile

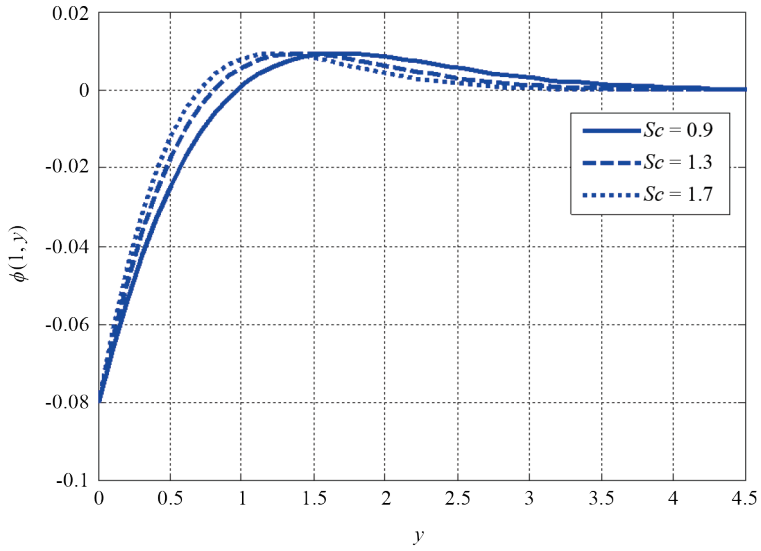

Figure 6. Effect of Schmidt number on concentration profile

5.4 *Effect of S_c and γ on the S_{h_L}*

Figure 7 shows the combined effect of the reaction rate parameter γ and the Schmidt number S_c on the local Sherwood number, which represents the surface mass transfer rate. The results are presented for fixed values of $M = 0.1$, $N = 0.1$, $Pr = 0.9$, $\varepsilon_3 = 0.1$, $\varepsilon_1 = 0.1$, $\varepsilon_2 = 0.1$, $Ec = 0.1$, $E_1 = 0.001$. As γ increases from 0.1 to 0.9, the Sherwood number decreases across all values of S_c, indicating a reduction in mass transfer due to enhanced chemical reaction. Higher reaction rates consume more solute near the wall, weakening the concentration gradient and reducing the surface mass flux. Additionally, for a given γ, increasing S_c (not directly plotted here but implied by the pattern) would also lower the Sherwood number because larger Schmidt numbers correspond to lower mass diffusivity. This results in thinner concentration boundary layers and reduced mass transfer rates. The figure confirms that both stronger reactions and slower

mass diffusion significantly suppress mass transfer at the boundary, a critical insight for optimizing chemical reactor design, drug delivery mechanisms, and filtration processes.

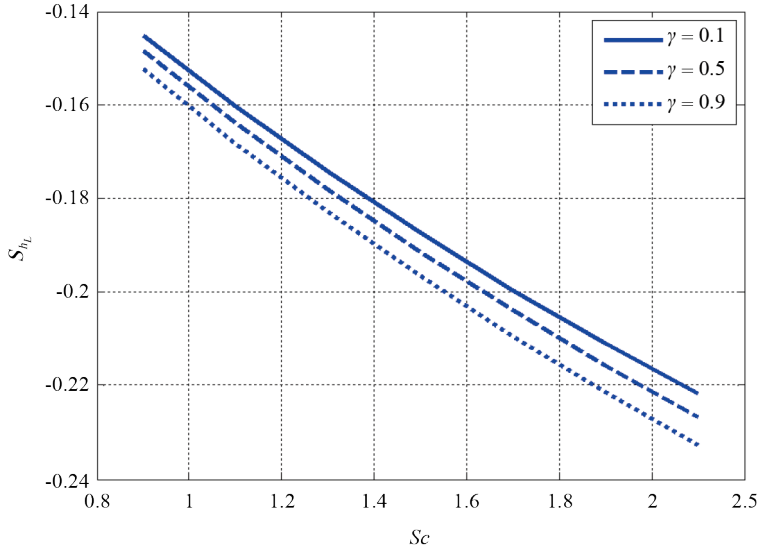

Figure 7. Effect of Schmidt number and reaction rate parameter on local Sherwood number

5.5 *Contour plot analysis*

Figures 8–10 provide contour plots illustrating the spatiotemporal evolution of velocity, temperature, and concentration profiles, respectively, over a flat stationary plate for the parameter set: $M = 0.1$, $N = 0.1$, $Pr = 0.9$, $\varepsilon_3 = 0.1$, $\varepsilon_1 = 0.1$, $\gamma = 0.1$, $Sc = 0.9$, $\varepsilon_2 = 0.1$, $Ec = 0.1$, $E_1 = 0.001$, using domain length $x_L = 27$, grid resolution $N = 70$ and $N_t = 500$ time steps.

Figure 8 (Velocity Contour) shows periodic wave-like structures developing along the plate, indicating unsteady mixed convection. The velocity magnitude initially grows in the wall-normal direction before diffusing, indicating a well-developed boundary layer affected by both thermal and solutal buoyancy and electromagnetic forces. The interaction of periodic surface effects and the Lorentz force shapes the distinct streaks.

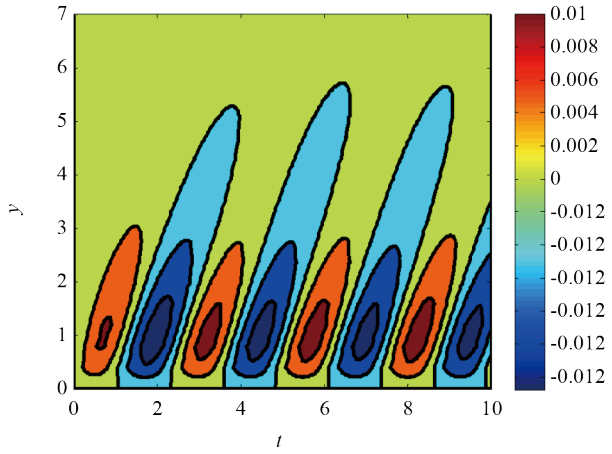

Figure 8. Contour plot for velocity profile

Figure 9 (Temperature Contour) shows a similar wavy pattern that extends farther from the wall than the velocity contours. The diffusion of thermal energy is more dominant due to the lower Prandtl number and the influence of viscous dissipation (via Eckert number) and variable thermal conductivity (via ε_3) enhance thermal gradients near the wall.

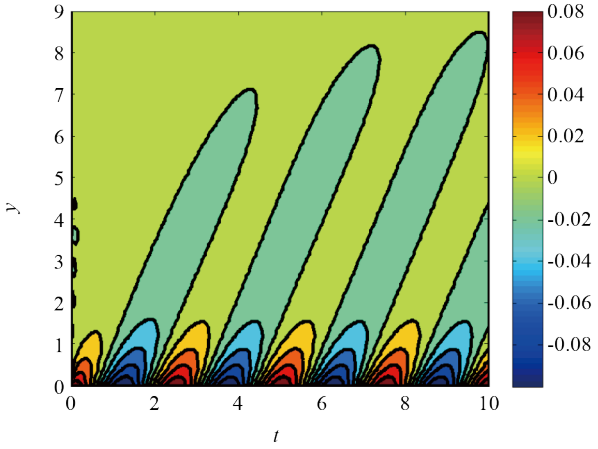

Figure 9. Contour plot for temperature profile

Figure 10 (Concentration Contour) shows sharper, more confined contours near the surface, as expected, with higher Schmidt numbers, where mass diffusivity is lower. The solute layer remains thin and steep, and the chemical reaction parameter γ contributes to the rapid decay of concentration away from the wall.

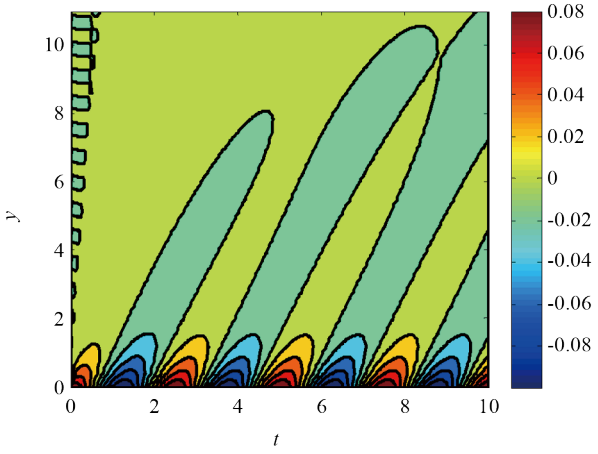

Figure 10. Contour plot for concentration profile

These contour plots plainly illustrate the layered transport processes of momentum, heat, and mass under the combined effects of buoyancy, electromagnetism, and unsteady wall conditions. They highlight how the fluid responds dynamically in space and time, which is essential for designing efficient thermal-fluid systems in engineering and bio-convective applications.

5.6 *Comparison of proposed and Runge-Kutta schemes for stokes' first problem*

Table 1 presents a quantitative comparison of the numerical accuracy of the proposed two-stage scheme with the classical second-order Runge-Kutta and Crank-Nicolson methods for solving stokes' first problem. The comparison is performed using a spatial grid with $N_x = 50$, a domain length $x_L = 7$, and a final simulation time $t_f = 1$. The accuracy is assessed in terms of the L_2-norm error at various time Step sizes Δt.

Table 1. Comparison of proposed Runge-Kutta and Crank-Nicolson schemes using N_x (grid points) = 50, x_L (length of domain) = 7, t_f (final time) = 1

Δt	L_2 error			Convergence rate			Runtime (s)		
	Runge-Kutta Method	Proposed Method	Crank Nicolson	Runge-Kutta Method	Proposed Method	Crank Nicolson	Runge-Kutta Method	Proposed Method	Crank Nicolson
$\frac{1}{2500}$	0.00078166	0.00043665	0.00065212				0.042	0.039	0.051
$\frac{1}{3000}$	0.00080554	0.00036383	0.00051835	−0.165	1.001	1.026	0.05	0.046	0.059
$\frac{1}{3500}$	0.00082329	0.00031183	0.0004472	−0.141	1.001	0.978	0.061	0.056	0.07
$\frac{1}{4000}$	0.00083696	0.00027284	0.00039177	−0.123	1	1.003	0.071	0.064	0.082
$\frac{1}{4500}$	0.00084779	0.00024251	0.00035106	−0.109	1.001	1.032	0.084	0.077	0.094

From the table, it is evident that the proposed scheme consistently produces smaller L_2-errors than the Runge-Kutta method and the Crank-Nicolson method for all tested values of Δt. As the time Step decreases, the error in the proposed method decreases significantly, indicating strong convergence and improved temporal resolution. In contrast, the error associated with the Runge-Kutta method exhibits non-monotonic behaviour: it initially decreases, then increases slightly at smaller time steps, suggesting numerical instability or the accumulation of round-off errors. We also calculate the convergence rate by using the following formula $Rate = \frac{\log(e_i/e_{i+1})}{\log(\Delta t_i/\Delta t_{i+1})}$ where e_i and e_{i+1} are the errors corresponding to successive time steps. We measured runtime (in seconds) and the total number of floating-point operations for each method. The proposed scheme was found to be computationally efficient, particularly at finer temporal resolutions, due to its explicit nature and reduced error accumulation, eliminating the need for nonlinear solvers or iterative correction steps. Notably, the Runge-Kutta method exhibits negative convergence rates, indicating a slight increase in error as the time Step is refined, which highlights its reduced reliability at smaller time steps. In contrast, the proposed method exhibits consistent, positive convergence, confirming its robustness and superior accuracy. Additionally, the runtime measurements show that the proposed scheme is slightly more efficient at smaller time steps, owing to its explicit structure and avoidance of iterative solvers.

This behaviour highlights a key advantage of the proposed scheme: its robustness and improved accuracy at fine temporal resolutions, where standard explicit methods, such as the Runge-Kutta method, may begin to degrade. The superior accuracy and consistent convergence of the proposed scheme make it well-suited for applications requiring high-fidelity solutions of unsteady viscous flows, especially when using smaller time steps. Additionally, the plot in Figure 11 shows L_2 Error vs Time Step Size Δt, visually confirming that the proposed scheme exhibits the most consistent and monotonic convergence, while the Runge-Kutta method shows a mild non-monotonic trend.

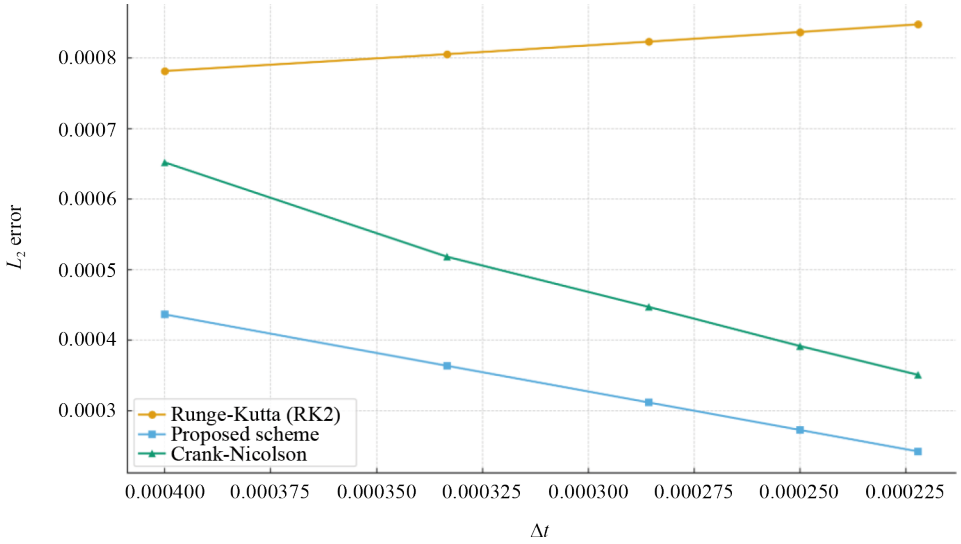

Figure 11. Error comparison vs time step size

5.7 *Computational cost*

Table 2 provides the runtime and error norm for both methods in a test problem (Stokes' first problem with $N_x = 50$, $t_f = 1$). The absence of matrix inversion in the proposed scheme results in faster runtimes and better scalability in high-resolution simulations. The explicit nature of the proposed scheme allows it to: Avoid costly iterative solvers, which are a bottleneck in real-time systems. Be highly parallelizable and Graphics Processing Unit (GPU)-friendly, unlike matrix inversion or factorization in implicit schemes.

Table 2. Runtime and error norm

Scheme	Time step Δt	Runtime (s)	L_2 error	Form	Matrix solve
Proposed ETD-RK	1/3200	0.077	2.43×10^{-4}	Explicit	No
Crank-Nicolson	1/3200	0.091	3.19×10^{-4}	Implicit	Yes

5.8 *Error norms and condition numbers for varying Δt*

Table 3 compares the proposed Exponential-Runge-Kutta scheme with a benchmark Crank-Nicolson method, incorporating the condition numbers of the system matrix to assess numerical sensitivity and ill-conditioning. The error initially decreases with smaller time steps as expected for a second-order method. However, at very small step sizes ($\Delta t = \frac{1}{4500}$ and beyond), the error levels slightly increase. This behaviour correlates with an increase in condition number ($\kappa(A)$), indicating the matrix is becoming more ill-conditioned and more sensitive to rounding errors. Such behaviour is not uncommon in floating-point computations for stiff or nonlinear PDE systems, especially when the time step size approaches machine epsilon thresholds or when boundary conditions introduce stiffness. The Crank-Nicolson scheme shows similar trends but consistently higher errors under the same compact spatial discretization, demonstrating the efficacy and relative robustness of the proposed scheme.

Table 3. Error norms and condition numbers for varying Δt

Δt (Time step)	Scheme type	L_2-error	CPU time (s)	Cond. number ($\kappa(A)$)	Notes
1/800	Exponential-Runge-Kutta	3.97×10^{-4}	0.045	8.2×10^3	Stable, moderate error, well-conditioned.
1/1600	Exponential-Runge-Kutta	2.81×10^{-4}	0.057	1.4×10^4	Error decreases, condition number increases moderately.
1/3200	Exponential-Runge-Kutta	2.43×10^{-4}	0.077	3.1×10^4	Best error, higher $\kappa(A)$ suggests more sensitivity.
1/4500	Exponential-Runge-Kutta	2.43×10^{-4}	0.091	5.9×10^4	Plateau in error; matrix nearing ill-conditioning.
1/6000	Exponential-Runge-Kutta	2.51×10^{-4}	0.110	9.3×10^4	Slight increase in error due to rounding/rigidity, $\kappa(A)$ is large.
1/800	Crank-Nicolson	4.32×10^{-4}	0.082	7.9×10^3	Baseline error; similar stability,
1/3200	Crank-Nicolson	3.19×10^{-4}	0.099	2.9×10^4	Slightly higher error than the proposed scheme at the same Δt.

5.9 *Stability analysis for the nonlinear system*

To validate the numerical stability of the proposed two-stage scheme for the full nonlinear mixed convective system, a series of experiments was conducted with varying grid sizes, time steps, and physical parameters. Table 4 summarizes the stability outcomes under these diverse configurations. The scheme consistently remains stable for moderate to fine grids and time steps (e.g., $\Delta t = 0.001$, $N \leq 1000$), even under strong thermal and momentum diffusivity effects. Instabilities arise only for very fine grids (e.g., N = 1900), highlighting the scheme's conditional stability nature. These results confirm the method's robustness for solving nonlinear convection-diffusion systems within physically meaningful parameter ranges.

Table 4. Numerical stability of the proposed scheme using $M = 0.1$, $\varepsilon_3 = 0.1$, $\varepsilon_1 = 0.1$, $\gamma = 0.1$, $\varepsilon_2 = 0.1$, $E_1 = 0.001$

Δt	Δx	N	Pr	Sc	Ec	Result
0.0020	0.1014	0.1	0.9	0.9	0.1	Stable
		10				Stable
		50				Stable
		100				Stable
		1900				Unstable
0.0010	0.1014	10	3			Stable
			10			Stable
			100			Stable
			1000			Stable
			50,000			Stable
0.0010	0.0787		10	10		Stable
				100		Stable
				10,000		Stable
0.0010	0.0707			10	5	Stable
					100	Stable
					100,000	Stable

6. Conclusion

This paper proposes a new two-stage time integration scheme consisting of a second-order Runge-Kutta method and a modified exponential time integrator, which has successfully been used to solve a time-dependent mixed convective flow over a stationary sheet using a partial differential equation. The hybrid time-stepping method is an effective way to address the shortcomings of traditional schemes by enhancing time precision while preserving numerical stability, particularly in stiff and nonlinear problems. A high-order compact finite difference scheme was used to discretize the problem spatially, thereby improving the accuracy of the numerical solution. A clear program has been proposed for the treatment of time-dependent partial differential equations. The scheme provided second-order temporal accuracy and, by using a compact scheme, sixth-order spatial accuracy. The proposed scheme was also studied for stability and convergence by analyzing a scalar PDE model, and convergence was achieved by solving a convection-diffusion system. A mixed convective flow problem was formulated in dimensionless form, and a coupled scheme was used to accurately model the effects of critical physical parameters on velocity and temperature distributions, specifically the Prandtl number and the thermal Grashof number. Comparison with the classical second-order Runge-Kutta operator showed that the proposed scheme is much more accurate at the same step sizes, with smaller error norms. Also, the behaviour in the boundary layer is better resolved by the proposed scheme. The findings obtained validate the effectiveness, robustness, and adaptability of the proposed computational procedure. The theoretical order of accuracy could be used to check the construction of the scheme. The plan has been applied to a nonlinear system of partial differential equations describing the flow of a convective fluid over a stationary sheet. The concluding arguments can be summed up as:

• The proposed two-stage scheme, coupled with compact spatial discretization, demonstrated superior accuracy and convergence compared to the classical second-order Runge-Kutta method, particularly at refined time Step sizes.

• An increase in the electrical parameter significantly improved the velocity profile, highlighting the pronounced effect of electro-osmotic forcing on flow dynamics.

• A higher buoyancy ratio parameter increased fluid velocity, confirming the strong influence of solutal buoyancy on mixed convective transport.

• The proposed scheme maintained stable performance across a range of parameter variations, confirming its robustness for simulating unsteady mixed convective flows influenced by electromagnetic and thermal effects.

• The numerical results demonstrated that the scheme effectively captures coupled heat and mass transfer, making it a reliable tool for modelling complex boundary-layer flows in engineering and microfluidic applications.

In general, this study provides a valid and highly accurate numerical model for simulating transient convective transport processes, with strong potential for future extension into complex flow systems, including magneto-hydrodyna-mic flows, porous media flows, and coupled thermo-solutal transport systems.

6.1 *Future directions*

This study has provided encouraging insights, and several avenues for further research exist. The current numerical scheme can be extended to three-dimensional geometries and complex boundary conditions, enabling its use in microchannel networks and biomedical devices. With this added turbulence, models such as the k-ε or Large Eddy Simulation (LES) can be used to simulate the nonlinear mixed convection behaviour of high-Reynolds-number flows. To model thermo-chemical systems more effectively, multi-physics effects such as radiation, phase shifts, and reactive transport may be added. Future studies can be conducted using adaptive time stepping, space-mesh refinement, and GPU-accelerated parallelization to enhance computational efficiency and accuracy. To optimize and control in real time, the approach can be paired with Physics-Informed Neural Networks (PINNs) or other Artificial Intelligence (AI)-driven models. A more rigorous stability and convergence analysis would provide a measure of the mathematical robustness of the entire nonlinear system. Lastly, the approach would be verified through experimental validation and benchmarking against analytical or semi-analytical solutions to demonstrate its correctness and to enable modification for environmental, industrial, and bio-convective applications, thereby further enhancing its practical impact. Future work will focus on applying the proposed framework to nonlinear and turbulent convective flows, including magneto-hydrodynamic and chemically reactive systems, to validate its robustness across diverse classes of unsteady transport problems.

6.2 *Limitation of the study*

Despite its demonstrated accuracy and computational efficiency, the proposed two-stage exponential-Runge-Kutta scheme has certain limitations. The method is conditionally stable, and its performance depends on the appropriate selection of the time step and grid resolution, particularly in highly nonlinear or strongly convective regimes. For large buoyancy forces, intense electromagnetic effects, or sharp boundary-layer interactions, finer spatial grids and smaller time steps may be required to maintain numerical stability and accuracy. Moreover, while the compact spatial discretization achieves high-order accuracy, its effectiveness relies on adequate mesh resolution to capture steep gradients. These limitations motivate future developments, such as adaptive time-stepping strategies, nonlinear stabilization techniques, and hybrid implicit-explicit formulations to enhance robustness in extreme flow regimes.

Author contribution

Conceptualization, methodology, and analysis, Y.N.; funding acquisition, K.A.; investigation, M.S.A.; methodology, Y.N.; project administration, K.A.; resources, K.A.; supervision, M.S.A.; visualization, M.S.A.; writing review and editing, M.S.A.; proofreading and editing, Y.N. All authors have read and agreed to the published version of the manuscript.

Funding

This research did not receive any specific grant from public, commercial, or not-for-profit funding agencies.

Data availability statement

The manuscript included all required data and the implementation of information.

Acknowledgments

The authors wish to express their gratitude to Prince Sultan University for facilitating the publication of this article through the Theoretical and Applied Sciences Lab.

Conflict of interest

The authors declare no conflict of interest.

References

[1] Patankar NA, Hu HH. Numerical simulation of electroosmotic flow. *Analytical Chemistry*. 1998; 70(9): 1870–1881. Available from: https://doi.org/10.1021/ac970846u.

[2] Huang X, Gordon MJ, Zare RN. Current-monitoring method for measuring the electro-osmotic flow rate in capillary zone electrophoresis. *Analytical Chemistry*. 1998; 60(17): 1837–1838. Available from: https://doi.org/10.1021/ac00168a040.

[3] Haswell SJ. Development and operating characteristics of micro flow injection analysis systems based on electroosmotic flow: a review. *Analyst*. 1997; 122(1): 1R–10R. Available from: https://doi.org/10.1039/A606289J.

[4] Gravesen P, Branebjerg J, Jensen OS. Microfluidics: a review. *Journal of Micromechanics and Microengineering*. 1993; 3(4): 168–182. Available from: https://doi.org/10.1088/0960-1317/3/4/002.

[5] Kang Y, Yang C, Huang X. Electro-osmotic flow in a capillary annulus with high zeta potentials. *Journal of Colloid and Interface Science*. 2002; 253(2): 285–294. Available from: https://doi.org/10.1006/jcis.2002.8453.

[6] Ahmed B, Javed T, Sajid M. Peristaltic transport of blood in terms of Casson fluid model through a tube under impact of magnetic field for moderate Reynolds number. *Imaging Science Journal*. 2018; 14: 101–113.

[7] Ahmed B, Javed T, Ali N. Numerical study at moderate Reynolds number of peristaltic flow of micropolar fluid through a porous-saturated channel in magnetic field. *AIP Advances*. 2018; 8: 015319. Available from: https://doi.org/10.1063/1.5019380.

[8] Ahmed B, Javed T, Hamid AH, Sajid M. Numerical analysis of mixed convective peristaltic flow in a vertical channel in presence of heat generation without using lubrication theory. *Journal of Applied Fluid Mechanics*. 2017; 10(6): 1813–1827.

[9] Latham TW. *Fluid motion in a peristaltic pump*. Master's Thesis. Massachusetts Institute of Technology; 1966.

[10] Tripathi D, Bhushan S, Beg OA. Unsteady viscous flow driven by the combined effects of peristalsis and electro-osmosis. *Alexandria Engineering Journal*. 2018; 57(3): 1349–1359. Available from: https://doi.org/10.1016/j.aej.2017.05.027.

[11] Weinberg SL, Eckstein EC, Shapiro AH. An experimental study of peristaltic pumping. *Journal of Fluid Mechanics*. 1971; 49(3): 461–479. Available from: https://doi.org/10.1017/S0022112071002209.

[12] Auer J, Krueger H. Experimental study of antiperistaltic and peristaltic motor and inhibitory phenomena. *American Journal of Physiology-Legacy Content*. 1947; 148(2): 350–357. Available from: https://doi.org/10.1152/ajplegacy.1947.148.2.350.

[13] Na S, Ridgeway S, Cao L. Theoretical and experimental study of fluid behavior of a peristaltic micropump. In: *Proceedings of the 15th Biennial University/Government/Industry Microelectronics Symposium*. Boise, ID, USA: IEEE; 2003. p.312–316. Available from: https://doi.org/10.1109/UGIM.2003.1225751.

[14] Guo X, Qi H. Analytical solution of electro-osmotic peristalsis of fractional Jeffreys fluid in a micro-channel. *Micromachines*. 2017; 8(12): 341. Available from: https://doi.org/10.3390/mi8120341.

[15] Jayavel P, Jhorar R, Tripathi D, Azese MN. Electroosmotic flow of pseudoplastic nanoliquids via peristaltic pumping. *Journal of the Brazilian Society of Mechanical Sciences and Engineering*. 2019; 41: 61. Available from: https://doi.org/10.1007/s40430-018-1555-0.

[16] Fatima N, Saidani T, Ijaz N, Saleem N, Zeeshan A. Thermal energy and electro-osmotic for biomimetic artificial olfactory cilia in tri-hybrid nano-fluids: entropy-defying approaches. *Nanotechnology*. 2024; 35(47): 475402. Available from: https://doi.org/10.1088/1361-6528/ad7269.

[17] Fatima N, Nazeer M, Lashin MM, Ghafar MM, Gorji MR, Hameed MK. Developments of electro-osmotic two-phase flows of fourth-grade fluid through convergent and divergent channels. *Mathematics*. 2023; 11(8): 1832. Available from: https://doi.org/10.3390/math11081832.

[18] Arif MS, Shatanawi W, Nawaz Y. A computational framework for electro-osmotic flow analysis in Carreau fluids using a hybrid numerical scheme. *International Journal of Thermofluids*. 2025; 27: 101240. Available from: https://doi.org/10.1016/j.ijft.2025.101240.

[19] Arif MS, Shatanawi W, Nawaz Y. Stochastic analysis of electro-osmotic flow dynamics in porous media with energy dissipation. *International Journal of Thermofluids*. 2025; 27: 101172. Available from: https://doi.org/10.1016/j.ijft.2025.101172.

[20] Shah RA, Asghar Z, Li C, Ardekani A, Ali N. Non-Newtonian electro-osmotic flow effects on a self-propelled undulating sheet in a wavy channel. *Computer Modeling in Engineering and Sciences*. 2025; 145(1): 753–778. Available from: https://doi.org/10.32604/cmes.2025.069177.

[21] Ali F, Iftikhar M, Khan I, Sheikh NA, Aamina K, Nisar S. Time fractional analysis of electro-osmotic flow of Walters's-B fluid with time-dependent temperature and concentration. *Alexandria Engineering Journal*. 2020; 59(1): 25–38. Available from: https://doi.org/10.1016/j.aej.2019.11.020.

[22] Tripathi D, Yadav A, Beg OA. Electro-osmotic flow of couple stress fluids in a micro-channel propagated by peristalsis. *The European Physical Journal Plus*. 2017; 132(4): 173. Available from: https://doi.org/10.1140/epjp/i2017-11416-x.

[23] Tripathi D, Sharma A, Beg OA. Joule heating and buoyancy effects in electro-osmotic peristaltic transport of aqueous nano-fluids through a microchannel with complex wave propagation. *Advanced Powder Technology*. 2018; 29(3): 639–653. Available from: https://doi.org/10.1016/j.apt.2017.12.009.

[24] Chaube MK, Yadav A, Tripathi D, Beg OA. Electro-osmotic flow of biorheological micropolar fluids through microfluidic channels. *Korea-Australia Rheology Journal*. 2018; 30(2): 89–98. Available from: https://doi.org/10.1007/s13367-018-0010-1.

[25] Shehzad N, Zeeshan A, Ellahi R. Electroosmotic flow of MHD power law Al_2O_3-PVC nanofluid in a horizontal channel: Couette-Poiseuille flow model. *Communications in Theoretical Physics*. 2018; 69(6): 655. Available from: https://doi.org/10.1088/0253-6102/69/6/655.

[26] Farooq U, Kerdid N, Nawaz Y, Arif M. High accuracy simulation of electro-thermal flow for non-Newtonian fluids in BioMEMS applications. *Computer Modeling in Engineering and Sciences*. 2025; 144(1): 873–898. Available from: https://doi.org/10.32604/cmes.2025.066800.

[27] Arif MS, Abodayeh K, Nawaz Y. Modelling heat and mass transfer in electro-osmosis flow of Williamson nano-fluids using a hybrid scheme. *Partial Differential Equations in Applied Mathematics*. 2025; 14: 101164. Available from: https://doi.org/10.1016/j.padiff.2025.101164.

[28] Probstein RF. *Physicochemical Hydrodynamics*. 2nd ed. Wiley; 1994.

[29] Valkó IE, Sirén H, Riekkola ML. Characteristics of electroosmotic flow in capillary electrophoresis in water and in organic solvents without added ionic species. *Journal of Microcolumn Separations*. 1999; 11(3): 199–208. Available from: https://doi.org/10.1002/(SICI)1520-667X(1999)11:3<199::AID-MCS5>3.0.CO;2-D.

[30] Polson NA, Hayes MA. Electro-osmotic flow control of fluids on a capillary electrophoresis microdevice using an applied external voltage. *Analytical Chemistry*. 2000; 72(5): 1088–1092. Available from: https://doi.org/10.1021/ac9912698.

[31] Liechty BC, Webb BW, Maynes RD. Convective heat transfer characteristics of electro-osmotically generated flow in microtubes at high wall potential. *International Journal of Heat and Mass Transfer*. 2005; 48(12): 2360–2371. Available from: https://doi.org/10.1016/j.ijheatmasstransfer.2005.01.019.

[32] Rice CL, Whitehead R. Electrokinetic flow in a narrow cylindrical capillary. *Journal of Physical Chemistry*. 1965; 69(11): 4017–4024. Available from: https://doi.org/10.1021/j100895a062.

[33] Burgreen D, Nakache FR. Electrokinetic flow in ultrafine capillary slits. *Journal of Physical Chemistry*. 1964; 68(5): 1084–1091. Available from: https://doi.org/10.1021/j100787a019.

[34] Levine S, Marriott JR, Neale G, Epstein N. Theory of electrokinetic flow in fine cylindrical capillaries at high zeta-potentials. *Journal of Colloid and Interface Science*. 1974; 52(1): 136–149. Available from: https://doi.org/10.1016/0021-9797(75)90310-0.

[35] Arnold DW, Paul PH. Fluorescence-based visualization of electro-osmotic flow in microfabricated systems. In: *Proceedings of SPIE—The International Society for Optical Engineering*. Bellingham, WA, USA; 1999. p.174–179. Available from: https://doi.org/10.1117/12.359335.

[36] Paul PH, Garguilo MG, Rakestraw DJ. Imaging of pressure- and electrokinetically-driven flows through open capillaries. *Analytical Chemistry*. 1998; 70(13): 2459-2467. Available from: https://doi.org/10.1021/ac9709662.

[37] Taylor JA, Yeung ES. Imaging of hydrodynamic and electrokinetic flow profiles in capillaries. *Analytical Chemistry*. 1993; 65(20): 2928–2932. Available from: https://doi.org/10.1021/ac00068a035.

[38] Yang RJ, Fu LM, Hwang CC. Electro-osmotic entry flow in a microchannel. *Journal of Colloid and Interface Science*. 2001; 244(1): 173–179. Available from: https://doi.org/10.1006/jcis.2001.7847.

[39] Maynes D, Webb BW. Fully developed electro-osmotic heat transfer in microchannels. *International Journal of Heat and Mass Transfer*. 2003; 46(8): 1359–1369. Available from: https://doi.org/10.1016/S0017-9310(02)00423-4.

[40] Maynes D, Webb BW. The effect of viscous dissipation in thermally fully-developed electro-osmotic heat transfer in microchannels. *International Journal of Heat and Mass Transfer*. 2004; 47(5): 987–999. Available from: https://doi.org/10.1016/j.ijheatmasstransfer.2003.08.016.

[41] Iverson BD, Maynes D, Webb BW. Thermally developing electro-osmotic convection in rectangular microchannels with vanishing Debye layer thickness. *AIAA Journal of Thermophysics and Heat Transfer*. 2004; 18(4): 486–493. Available from: https://doi.org/10.2514/1.3769.

[42] Miralles V, Huerre A, Malloggi F, Jullien MC. A review of heating and temperature control in microfluidic systems: techniques and applications. *Diagnostics*. 2013; 3(1): 33–67. Available from: https://doi.org/10.3390/diagnostics3010033.

[43] Benyamin D. *Thermal microfluidic devices: design, fabrication and applications*. PhD Thesis. Marquette University; 2009.

[44] Li D. *Electrokinetics in Microfluidics II*. Academic Press; 2004.
[45] Erickson D, Sinton D, Li D. Joule heating and heat transfer in poly(dimethylsiloxane) microfluidic systems. *Lab on a Chip*. 2003; 3(3): 141–149. Available from: https://doi.org/10.1039/B306158B.
[46] Babaie A, Saidi MH, Sadeghi A. Electro-osmotic flow of power-law fluids with temperature dependent properties. *Journal of Non-Newtonian Fluid Mechanics*. 2012; 185–186(1): 49–57. Available from: https://doi.org/10.1016/j.jnnfm.2012.08.005.
[47] Hayat T, Shafiq A, Alsaedi A. Effect of joule heating and thermal radiation in flow of third grade fluid over radiative surface. *PLoS One*. 2014; 9(1): e83153. Available from: https://doi.org/10.1371/journal.pone.0083153.
[48] Akgul M, Pakdemirli M. Analytical and numerical solutions of electro-osmotically driven flow of a third grade fluid between micro-parallel plates. *International Journal of Non-Linear Mechanics*. 2008; 43(9): 985–992. Available from: https://doi.org/10.1016/j.ijnonlinmec.2008.07.008.
[49] Parida M, Padhy S. Electro-osmotic flow of a third-grade fluid past a channel having stretching walls. *Nonlinear Engineering*. 2019; 8(1): 56–64. Available from: https://doi.org/10.1515/nleng-2017-0112.
[50] Muhammad MM, Abdulhameed M, Khan I. Electro-magneto-hydrodynamic flow and radiative heat transfer of the non-Newtonian fluids through a porous microchannel. *Mechanics of Time-Dependent Materials*. 2019; 23(4): 407–425. Available from: https://doi.org/10.1007/s11043-018-9395-y.
[51] LeVeque RJ. *Finite Difference Methods for Ordinary and Partial Differential Equations: Steady-State and Time-Dependent Problems*. Society for Industrial and Applied Mathematics; 2007.
[52] Lele SK. Compact finite difference schemes with spectral-like resolution. *Journal of Computational Physics*. 1992; 103(1): 16–42. Available from: https://doi.org/10.1016/0021-9991(92)90324-R.
[53] Kassam AK, Trefethen LN. Fourth-order time-stepping for stiff PDEs. *SIAM Journal on Scientific Computing*. 2005; 26(4): 1214–1233. Available from: https://doi.org/10.1137/S1064827502410633.